Title: Optimization of systemic AAV9 gene therapy in Niemann-Pick disease, type C1 mice

Running Title: Systemic AAV9 gene therapy in *Npc1*^{m1N} mice

Summary Blurb: Systemic AAV9-h*NPC1* gene therapy in null *Npc1*^{m1N} mice at higher doses or with earlier administration and treatment of hypomorphic *Npc1*^{I1061T} mice delays disease progression and increases lifespan.

Authors: Avani V. Mylvara[1,2*], Alana L. Gibson[2,3*], Tansy Gu[2,4*], Cristin D. Davidson[1,2+], Arturo A. Incao[2], Katerina Melnyk[1], Susan R. Gembic[1], Dominick Pierre-Jacques[5], Stephanie M. Cologna[5], Charles P. Venditti[2], Forbes D. Porter[1], William J. Pavan[2]

[1]*Eunice Kennedy Shriver* National Institute of Child Health and Human Development, National Institutes of Health, Department of Human Health and Services, Bethesda, MD; [2]National Human Genome Research Institute, National Institutes of Health, Department of Human Health and Services, Bethesda, MD; [3]Howard Hughes Medical Institute, Department of Cellular and Molecular Medicine, Section of Neurobiology, Division of Biological Sciences, University of California, San Diego, San Diego, CA; [4]University of North Carolina, Chapel Hill, NC; [5]University of Illinois Chicago, Chicago, IL
*Indicates equal contribution

Author Contributions

- AVM – data curation, formal analysis, investigation, methodology, validation, visualization, writing – original draft, writing – reviewing & editing (0000-0002-8741-4008)
- ALG – data curation, formal analysis, investigation, validation, writing – reviewing & editing (0000-0003-2247-7064)
- TG – data curation, formal analysis, investigation, validation, writing – reviewing & editing (0000-0002-0653-0892)
- CDD – conceptualization, data curation, investigation, project administration, supervision, validation, visualization, writing – original draft, writing – reviewing & editing (0000-0002-5508-8113)
- AAI – investigation, methodology (0000-0001-6801-4562)
- KM – formal analysis, investigation, validation, visualization, writing – reviewing & editing (0000-0001-9167-5801)
- SG – formal analysis, investigation, validation, writing – reviewing & editing
- DP-J – data curation, formal analysis, investigation, methodology, visualization, writing -reviewing & editing (0009-0009-1272-0607)
- SMC – conceptualization, funding acquisition, methodology, project administration, resources, supervision, writing – reviewing & editing (0000-0002-3541-3361)
- CPV – methodology, ideas, writing – reviewing & editing (0000-0001-6599-1253)
- FDP – project administration, supervision, funding acquisition, resources, writing – review & editing (0000-0001-9397-0046)
- WJP – conceptualization, project administration, supervision, funding acquisition, resources (0000-0001-8281-5120)

[+]Corresponding Author (Cristin Davidson)

Abstract:

Niemann-Pick disease, type C1 (NPC1) is a rare, fatal neurodegenerative disorder caused by pathological variants in *NPC1*, which encodes a lysosomal cholesterol transporter. FDA-approved treatments are limited and do not target the underlying genetic defect. Both systemic and central nervous system (CNS) delivery of AAV9-h*NPC1* have shown significant disease amelioration in NPC1 murine models. To assess the impact of dose in null $Npc1^{m1N/m1N}$ mice, we systemically administered three different doses of AAV9-h*NPC1* at 4 weeks old. Then, to assess the impact of age, we administered the medium dose before phenotypic onset or at early- or late-stage of disease progression (4, 6 or 8 weeks old, respectively). Higher vector doses and earlier treatment were associated with significantly increased lifespan, slower disease progression, and enhanced CNS transduction. In $Npc1^{I1061T/I1061T}$ mice, a model recapitulating a common human hypomorphic variant, similar benefits ensued. Our findings help define dose ranges, treatment ages, and efficacy in hypomorphic models of NPC1 deficiency and suggest that higher doses of AAV9-h*NPC1* in pre-symptomatic disease states are likely to yield better outcomes in NPC1 individuals.

Introduction:

Niemann-Pick disease, type C (NPC) is a rare, fatal neurodegenerative disease with an incidence of ~1 in 100,000 live births [1]. This autosomal recessive lysosomal storage disorder is marked by unesterified cholesterol and sphingolipid accumulation in the lysosome, the latter of which is especially prominent in neural tissue. At least 95% of NPC1 individuals have disease associated variants in the integral membrane-bound NPC1 protein located in the lysosome (NPC1 disease, OMIM #257220). The remaining individuals have pathological variants in the NPC2 protein (NPC2 disease, OMIM #607625), a soluble lysosomal protein that transfers unesterified cholesterol to NPC1 [2]. Clinical presentation of both forms of the disease are similar, where loss of function of NPC1 or NPC2 results in intracellular accumulation of unesterified cholesterol and glycosphingolipids [1, 3-7]. Disease severity and onset is highly variable, affecting infants, children, and adults; however, the classical presentation of NPC1 is most often observed in school-age children and typically includes progressive cerebellar ataxia, vertical supranuclear gaze palsy, gelastic cataplexy, motor deficits, and cognitive impairment as well as visceral manifestations like hepatosplenomegaly [8, 9]. Miglustat, a glycosphingolipid synthesis inhibitor, is approved for treatment for NPC outside the US. Until recently, there were no Food and Drug Administration (FDA) approved therapies for NPC individuals. Then, in September 2024, the FDA approved arimoclomol (Miplyffa, in combination with miglustat) and levacetylleucine (Aqneursa) [10]. Though these and other investigational therapeutics provide some amelioration, all fail to address the root cause of the disorder – the absence of functional NPC1 protein that leads to morbidity and mortality [11-15]. Gene therapy can provide replacement of the dysfunctional NPC1 protein to treat the disease [16, 17].

Many studies have demonstrated that adeno-associated viral (AAV) gene therapy can successfully treat monogenic and rare diseases in pre-clinical models [18-23]. AAVs are already approved for treatment of individuals with disorders such as Spinal Muscular Atrophy (SMA1; onasemnogene abeparvovec-xioi [24-26]), RPE65 mutation associated retinal dystrophy (voretigene neparvovec-rzyl [27, 28]), and aromatic L-amino acid decarboxylase (AADC; eladocagene exuparvovec-tneq [29]). AAV9 is well documented to cross the blood-brain barrier (BBB) and transduce cells of the central nervous system (CNS) [30-34]. Given the devastating neurological impact of NPC1, gene therapy targeting the CNS is imperative. Of note, AAV9 also transduces multiple other organ systems, including the liver and peripheral nerves, that are implicated in NPC1 disease [8, 9, 35-41].

We and others have previously demonstrated that AAV9 vectors can effectively improve survival and delay disease progression in the null $Npc1^{m1N/m1N}$ ($Npc1^{m1N}$, single allele notation for homozygosity) murine model of NPC1 deficiency [18, 42-46]. $Npc1^{m1N}$ mice have a premature stop codon in the *Npc1* gene,

leading to the production of truncated, non-functional NPC1 protein and resulting in a severe disease phenotype [18, 42-51]. Both direct CNS administration (intracerebroventricular or intracisternal magna) [43, 45] and systemic administration (retro-orbital or intracardiac) [18, 42, 44] have successfully ameliorated disease in these mice. Greater success has been noted when using dual routes of CNS administration or administering higher doses of vector to the CNS [45, 46]. We and others have demonstrated that ubiquitous promoters provide greater disease correction in *Npc1*^{m1N} mice as compared to neuron-specific promoters [18, 46]. Further optimization studies have highlighted the therapeutic potential of novel capsids to improve CNS transduction [44].

Many preclinical gene therapy studies in *Npc1*^{m1N} mice have targeted neonates [42, 43, 45, 46]. Previously, we administered AAV9 vectors at 4 weeks old, before onset of phenotypic signs [18, 44]. The question remains whether late(r) intervention can still be effective following diagnoses in individuals after disease onset. Previous clinical studies for aromatic L-amino acid decarboxylase deficiency, a rare pediatric genetic disorder, suggest that AAV gene therapy is universally beneficial but treatment at a younger age was associated with greater benefits [29]. Intervention prior to clinical onset of neurologic symptoms in NPC is currently challenging because NPC1 is not routinely screened for in newborns and the average diagnostic delay remains ~4.1 years [52-55]. However, early intervention prior to neurological onset might be possible in familial cases and after diagnosis when there is infantile presentation with fetal ascites and liver disease [1, 56-58].

More than 600 pathogenic or likely pathogenic NPC1 variants have been described, most of which are missense mutations [59-61]. One of the most prevalent variants is a missense mutation resulting in an amino acid substitution (p.I1061T). The NPC1 p.I1061T protein misfolds and undergoes endoplasmic reticulum associated degradation (ERAD) [62-64]. A knock-in, hypomorphic *Npc1*^{I1061T} allele was generated to recapitulate the human disorder and results in a slightly protracted disease course compared to the more severe *Npc1*^{m1N} mouse model [65]. To assess whether residual NPC1 protein with compromised stability affected gene therapy treatment, we evaluated efficacy of gene therapy in *Npc1*$^{I1061T/I1061T}$ mice (*Npc1*^{I1061T}, single allele notation for homozygosity). We investigated and confirmed that residual NPC1 protein with compromised stability did not interfere with the efficacy of gene therapy.

In this paper we build on our previous work [18, 44], using systemic administration of an AAV9-elongation factor 1α (shortened)-h*NPC1* (AAV9-EF1a(s)-h*NPC1*) vector to treat NPC1 mice. We examine the therapeutic efficacy of this vector across different doses, at timepoints later in disease progression, and in *Npc1*^{I1061T} mice. Our results provide foundational preclinical data for the advancement of AAV9-EF1a(s)-h*NPC1* as a disease modulating therapy for individuals with NPC1 deficiency.

Results:

Dose selection and administration paradigm

Dose selection was based on our previously published work [18, 44], with vector genomes (vg) administered per mouse as the primary parameter. For consistency with other research and clinical trials, doses are also provided in terms of vg/kilogram (vg/kg). The medium dose administered at 4 weeks ($1.2x10^{12}$ vg or $1.28x10^{14}$ vg/kg) served as the baseline comparator across all studies. Lower and higher doses were chosen to capture a comprehensive dose-response range, considering both experimental and practical constraints which include the vector concentration coupled with our Animal Care and Use Committee's approved volumes for RO delivery. The medium dose was selected for the age at treatment study to ensure sufficient vector was available for full study enrollment.

Npc1^{m1N} mice treated with higher doses of AAV9-EF1a(s)-h*NPC1* show increased survival and delayed disease progression

All mice received a single retro-orbital injection of AAV9-EF1a(s)-h*NPC1* (referred to as AAV9), and each figure panel following includes data from 4-28 mice per group. Regarding statistical analyses, no significant differences between sex were found for any readout measure in the dose, age at treatment, or hypomorphic Npc1 model sub studies. Thus, data from males and females are combined in all statistical tests. The only exception to sex differences is weight curves, which were not analyzed. In this section, mice were sacrificed either at 10 weeks for an age-matched cohort or at humane endpoint for survival.

To compare the efficacy of AAV9 at different doses, mice were injected at 4 weeks old with either low ($1x10^{11}$ vg or $7.87x10^{12}$ vg/kg), medium ($1.2x10^{12}$ vg or $1.28x10^{14}$ vg/kg), or high ($4.3x10^{12}$ vg or $3.06x10^{14}$ vg/kg) dose. A Log-Rank, Mantel Cox test, with Bonferroni's correction for multiple comparisons was used to assess survival (Fig 1A, Table S2A). High- and medium-dose mice had a longer median survival (34.6 and 21.5 weeks, respectively) compared to low-dose (11.4 weeks) and saline-injected mice (10.6 weeks) (for all, $p < 0.0001$). Notably, even the low-dose group had improved survival compared to the saline-injected group (11.4 vs 10.6 weeks, $p = 0.005$).

To determine the effect of AAV9 dose on neurological disease progression, a composite phenotype score was assessed at 3-week intervals from 6 to 18 weeks, where increasing scores indicate disease progression (Fig 1B) [66]. The five neurological phenotypic parameters evaluated for the composite score include hindlimb clasp, motor function, kyphosis, balance, and grooming. High-dose mice showed greatest delay in disease progression, followed by medium dose mice, while low-dose mice mirrored the saline-injected mice (Fig 1B). Two-way ANOVA with mixed effects analysis and Tukey's multiple comparisons test was used to assess differences between groups (Table S3A). Between 6 and 9 weeks, the saline and low-dose groups had similar phenotype scores ($p = 0.95$), while the medium-dose and high-dose groups had significantly lower phenotype scores compared to the saline group (medium-dose: $p = 0.020$, high-dose: $p < 0.0001$) and the low-dose group (medium-dose: $p = 0.007$, high-dose: $p < 0.0001$). Notably, high-dose mice were not significantly different from *Npc1*$^{+/+}$ mice ($p = 0.91$). From 9 to 12 weeks, medium- and high-dose mice continued to show significantly lower phenotype scores than saline-injected and low-dose mice (for all, $p < 0.0001$). High-dose mice maintained lower phenotype scores closer to *Npc1*$^{+/+}$ mice ($p = 0.51$). From 15 to 18 weeks, high-dose mice had significantly lower phenotype scores than medium-dose mice ($p = 0.008$) and did not differ significantly from *Npc1*$^{+/+}$ mice ($p = 0.11$).

Npc1^{m1N} mice exhibit marked weight loss starting at about 6 weeks old. To evaluate disease onset, we assessed the week that mice reached peak weight (Fig 1C) and to evaluate disease progression, we assessed change in weight from 6 to 9 weeks (Fig 1D). Low-dose mice reached peak weight at a similar time to saline-injected mice (6.9 ± 0.6 weeks and 6.8 ± 0.7 weeks, respectively). In contrast, medium dose mice reached peak weight significantly later (11.3 ± 3.9 weeks) than saline-injected ($p = 0.0007$) or low-dose mice ($p = 0.007$). Similarly, high-dose mice reached peak weight significantly later (14.8 ± 3.1 weeks) than saline-injected ($p < 0.0001$) or low-dose mice ($p = 0.0003$). Statistical significance for week of peak weight was determined using a Kruskal-Wallis Test with Dunn's multiple comparisons test. Longitudinal weight data further demonstrates that mice maintain weight and survive longer as the dose of AAV9 increases (Fig S1A, B; Table S4A). When assessing percent weight change from 6 to 9 weeks (Fig 1D), both saline-injected and low-dose mice showed similar percent weight loss (-14.6% ± 6.8% and -9.0% ± 11.7%, respectively; $p = 0.64$) (Fig 1D). In contrast, medium-dose (11.2% ± 13.1%) and high-dose (15.3% ± 10.9%) mice showed significant weight gain compared to both saline-injected and low-dose groups (for all, $p < 0.0001$). Medium-dose and high-dose mice gained weight similarly to *Npc1*$^{+/+}$ mice (5.6% ± 4.1%) during this period (medium-dose: $p = 0.38$, high-dose: $p = 0.15$). Statistical significance for weight change from 6 to 9 weeks was assessed using one-way ANOVA with Tukey's multiple comparisons test.

Higher doses of AAV9 enhance viral transduction in brain and liver of *Npc1*^{m1N} mice

To evaluate the efficacy of vector transduction across tissues, droplet digital PCR (ddPCR) was performed on cerebellar (Fig 2Ai, iii), cerebral (Fig 2Bi, iii) and liver tissues (Fig 2Ci, iii) to assess h*NPC1* copy number at 10 weeks of age or at humane endpoint/survival. In parallel, Western blots were performed to measure NPC1 protein levels present in cerebellum (Fig 2Aii), cerebrum (Fig 2Bii), and liver (Fig 2Cii), as NPC1 protein presence is exclusively attributed to vector transduction in *Npc1*^{m1N} mice.

At 10-weeks-old, high-dose mice exhibited higher h*NPC1* copy numbers in the cerebellum (Fig 2Ai), cerebrum (Fig 2Bi), and liver (Fig 2Ci) compared to all other groups. Similar trends were observed in the spleen, kidney, lung, muscle, and brain stem (Fig S2).

In the cerebellum (Fig 2Aii) and cerebrum (Fig 2Bii), NPC1 protein levels were low, but detectable in high-dose mice and *Npc1*$^{+/+}$ mice, with higher levels observed in *Npc1*$^{+/+}$. In the liver (Fig 2Cii), NPC1 protein was detected only in *Npc1*$^{+/+}$, high-dose, and medium-dose mice, with high-dose mice showing higher average NPC1 protein expression than *Npc1*$^{+/+}$ mice. Representative western blots are shown in Fig S3.

In a linear regression analysis, lifespan was significantly associated with h*NPC1* copy number in the cerebellum and cerebrum within the medium dose group (Fig 2Aiii, Biii). However, two mice with exceptionally high copy numbers in these regions drove significance. In the liver, copy number did not predict lifespan in any individual treatment group (Fig 2Cii, linear regression analysis).

Higher doses of AAV9 reduce cerebellar and hepatic pathology in 10-week-old *Npc1*^{m1N} mice

Cerebellar ataxia is a major clinical feature in NPC individuals and is recapitulated in NPC1 mice with cerebellar pathology and Purkinje neuron degeneration [8, 51, 67]. To assess cholesterol storage and pathological alterations, we performed immunofluorescence staining of the cerebellum in 10-week-old mice. Parallel western blot analysis was used for quantification.

Unesterified cholesterol storage, as visualized by filipin labeling [68], is increased in NPC1 disease [69]. However, high dose gene therapy appears to moderately reduce cholesterol storage compared to other treated or saline-injected mice (Fig 3A). Reactive astrocytosis (GFAP positive staining) is a characteristic finding in both human and mice with NPC1 disease [70-72]. Treatment with AAV9 shows a mild dose-dependent decrease in astrocytosis (Fig 3A). GFAP protein levels do not appear to differ between saline-injected, low-, medium-, or high-dose mice (Fig 3C, representative blot Fig S4A,B).

Progressive loss of Purkinje neurons, particularly from anterior to posterior cerebellar lobules, is a hallmark of NPC1 disease [51, 67] and one with which our data align. Purkinje neuron survival (Calbindin D labeling) appears to improve with increasing doses of AAV9 and correlates with h*NPC1* copy number. Nevertheless, presence of Purkinje neuron remains markedly reduced compared to healthy *Npc1*$^{+/+}$ mice (Fig 3A). A similar dose-dependent increase is observed with Calbindin D protein levels, though levels remain below those of *Npc1*$^{+/+}$ mice (Fig 3D, representative blot Fig S4D,E).

Microglial activation, a well-documented feature of NPC1 pathology [72, 73], appears mildly reduced in high-dose mice, particularly in posterior cerebellar lobules as shown by IBA1 staining (Fig 3B). This reduction is accompanied by a decrease in CD68 protein levels in high-dose mice, a marker of reactive microglia [74] (Fig 3E, representative blot Fig S4B,C).

Hepatomegaly is a common feature of NPC1 disease, with infantile presentation often associated with liver disease [53, 57, 58]. To evaluate liver involvement, we performed immunohistochemical (Fig 4A) and immunofluorescence (Fig 4C) staining of macrophages using CD68 labeling [75] in 10-week-old mice. High- and medium-dose AAV9 treated mice showed a reduced percentage of CD68+ area compared to low-dose and saline-injected mice (Fig 4B, representative images 4A). Additionally, immunofluorescence staining demonstrated a decrease in cholesterol storage (filipin labeling) and macrophage presence (CD68) as the dose of AAV9 increased (Fig 4C).

AAV9 modulates sphingolipid accumulation in the brains of 10-week-old *Npc1^{m1N}* mice

In addition to cholesterol accumulation, multiple lipid classes exhibit altered levels in the NPC1 deficient brain due to impaired NPC1 protein function in mice [76-78]. Among these, gangliosides such as GM2 accumulate in the brains of *Npc1^{m1N}* mice [79]. Mass spectrometry imaging was used to assess the impact of AAV9 dose on sphingolipid distribution in 10-week-old *Npc1^{m1N}* mice and *Npc1$^{+/+}$* mice (Figure S5). While *Npc1$^{+/+}$* mice demonstrated little to no ganglioside accumulation, *Npc1^{m1N}* mice displayed high accumulation in the frontal cortex and cerebellar lobule X. Increasing AAV9 doses led to a qualitative reduction in ganglioside accumulation in both regions (Fig S5Ai). However, quantitative analysis of GM2 (d36:1) levels did not reveal statistically significant differences between groups (Fig S5B).

Beyond gangliosides, sphingolipid distribution is broadly disrupted in *Npc1^{m1N}* mice, with altered distribution of hexosylceramides and dihydroceramides in the cerebellum [80]. Hexosylceramide (HexCer 46:4;O3) levels appeared lower in the cerebellum of *Npc1^{m1N}* mice compared to *Npc1$^{+/+}$* mice. AAV9 treatment was associated with a qualitative increase in HexCer abundance in a dose-dependent manner, particularly in the rostral cerebellar lobules (lobules I-V) (Figure S5BAii). Conversely, dihydroceramide (Cer 32:2;O3) levels appeared elevated in the cerebellum of *Npc1^{m1N}* mice compared to *Npc1$^{+/+}$* mice. While AAV9 had a less pronounced effect on dihydroceramide accumulation, a visual trend towards reduction was observed at medium and high doses (Figure S5Aiii).

AAV9 treatment at 4-weeks improves survival and delays disease progression in *Npc1^{m1N}* compared to treatment at 6- or 8- weeks of age

Npc1^{m1N} mice were treated with 1.28×10^{14} vg/kg of AAV9 at 4 weeks (before onset of neurologic symptoms, hereafter referred to as pre-symptomatic), 6 weeks (early-stage disease), or 8 weeks (late-stage disease) to assess impact of treatment age on therapeutic efficacy. Disease onset is typically observed in *Npc1^{m1N}* mice at 6 weeks, with key manifestations including changes in motor coordination and ataxia that progress until death at approximately 10.6 weeks [66]. For this comparison, mice were sacrificed at 9 weeks to obtain age-matched cohorts or at humane endpoint for survival comparison.

Mice injected at 4 weeks exhibited a significantly longer median survival of 21.5 weeks compared to saline-injected mice (10.6 weeks, $p < 0.0001$) and those treated at 6 weeks (13.2 weeks, $p = 0.003$) or 8 weeks (11.9 weeks, $p < 0.0001$) (Fig 5A). Additionally, mice treated at 6 weeks survived significantly longer than both saline-injected mice ($p < 0.0001$) and mice treated at 8 weeks ($p = 0.0003$), while mice treated at 8 weeks survived longer than saline-injected mice ($p = 0.0006$). Statistical analysis was performed using the Log-Rank Mantel-Cox test with Bonferroni's correction for multiple comparisons, with detailed results provided in Table S2B.

Composite phenotype was assessed between 6 and 18 weeks to evaluate the effect of age of treatment on neurological disease progression (Fig 5B). Between 6 and 9 weeks of age, mice treated at 4 weeks old exhibited significantly lower phenotype scores compared to those at 6 and 8 weeks ($p = 0.001$, $p < 0.0001$

respectively), which progressed similarly ($p = 0.51$). From 9 to 12 weeks, the 4-week group maintained significantly lower composite scores than saline-injected mice ($p < 0.0001$), the 6-week group ($p = 0.0002$), and the 8-week group ($p < 0.0001$), but were higher than *Npc1*$^{+/+}$ mice ($p < 0.0001$). Two-way ANOVA with mixed effects analysis with Tukey's multiple comparisons test were used for statistical analysis, with detailed results presented in Table S3B.

To assess disease onset and progression, we evaluated week of peak weight and percent weight change between 6 and 9 weeks. Mice treated at 4 weeks reached peak weight significantly later (11.3 ± 3.9 weeks) than saline-injected mice (6.8 ± 0.7 weeks, $p = 0.003$) and those treated at 6 weeks (6.8 ± 2.3 weeks, $p < 0.001$) or 8 weeks (6.7 ± 0.6 weeks, $p < 0.001$) (Fig 5C, Kruskal-Wallis with Dunn's multiple comparisons test). In contrast, mice treated at 6 and 8 weeks reached peak weight at similar times as saline-injected mice ($p = 0.82$ and $p > 0.99$, respectively).

When evaluating percent weight change from 6 to 9 weeks, mice injected at 4 weeks (11.2% ± 13.1%) and *Npc1*$^{+/+}$ mice (6.0% ± 4.1%) exhibited weight gain and were significantly different from all other groups ($p < 0.0001$ for all comparisons). In contrast, *Npc1*^{m1N} mice injected at 6 or 8 weeks exhibited weight loss (-12.2% ± 7.7%, -20.0% ± 10.9%, respectively), which was not significantly different from saline-injected *Npc1*^{m1N} mice (-14.6% ± 6.8%; $p = 0.94$, $p = 0.44$, respectively) (Fig 5D, One-way ANOVA with Tukey's multiple comparisons test). Longitudinal weight data further indicate that both male and female cohorts treated earlier maintained weight and survived longer (Fig S2C,D; Table S4B).

Age of treatment affects AAV9 transduction in the cerebellum and treatment at 4 weeks reduces cerebellar pathology in 9-week-old *Npc1*^{m1N} mice

h*NPC1* copy number in the cerebellum was assessed in 9-week-old mice. Mice injected at 4 and 6 weeks had higher h*NPC1* copy numbers than saline mice or mice injected at 8 weeks (Fig 6A). NPC1 protein levels were similar across all treated mice (Fig 6B, representative blot Fig S6A,B).

Immunofluorescence staining and Western blots were utilized to evaluate cerebellar pathology in age-matched mice. Mice treated at 4 weeks demonstrated greater Purkinje neuron survival in anterior lobules and the entire cerebellum when compared to saline-injected mice and those treated at 6 or 8 weeks (Fig 6C); this pattern is also consistent with increased Calbindin D protein levels in mice treated at 4 weeks (Fig 6E, representative blot Fig S6A,B). Further, microgliosis appears mildly reduced in the posterior lobules of the cerebellum in the 4-week group compared to saline-injected and other treated mice (IBA1 labeling, Fig 6D). A similar reduction was observed in CD68 protein levels in the 4-week group, indicating decreased reactive microglial activity (Fig 6F, representative blot Fig S6C,D). Finally, GFAP protein levels (reactive astrocytosis) appear similar across all groups (Fig 6G, representative blot Fig S6C,D).

Age of treatment impacts AAV9 transduction in cerebrum and liver of *Npc1*^{m1N} mice

h*NPC1* copy number in the cerebrum and liver was also assessed via ddPCR in the age-matched cohort (9 weeks) and at humane endpoint. In the age-matched cohort, mice injected at 8 weeks exhibited the highest h*NPC1* copy number in the cerebrum compared to all other groups (Fig 7A). In the cerebrum, high copy numbers in 4- and 6-week-old injected groups were associated with longer lifespans based on linear regression analysis; however, two mice with exceptionally high copy numbers in the 4-week group drive significance in this finding. In mice treated at 8 weeks, copy number did not predict lifespan (Fig 7B).

In the livers of the age-matched cohort, mice treated at 8 weeks again had higher h*NPC1* copy numbers than other treated and saline-injected mice (Fig 7C). Linear regression analysis shows that higher copy

numbers in the liver predicted lifespan only in mice treated at 6-weeks old (Fig 7D). In mice from the age-matched cohort, immunohistochemical staining revealed a reduced presence of CD68+ macrophages in the liver of mice treated at 6 weeks compared to other treated and saline-injected mice (Fig 7F; representative images Fig 7E).

Npc1^{I1061T} mice treated with AAV9 show improved lifespan and delayed disease progression

To evaluate efficacy of AAV9 in a hypomorphic mouse model of NPC1 deficiency, *Npc1*^{I1061T} mice were treated with $1.28x10^{14}$ vg/kg ($1.2x10^{12}$ vg per mouse) of AAV9 at 4 weeks old. In this sub study, mice were sacrificed at 14 weeks for an age-matched cohort or humane endpoint for survival.

AAV9 treated *Npc1*^{I1061T} mice had a median survival of 22.9 weeks, significantly longer than the 15.0 weeks observed in saline-injected mice (Fig 8A, Log-Rank Mantel-Cox test, $p < 0.0001$). Previous studies report a median survival of about 17.9 weeks for *Npc1*^{I1061T} mice, while *Npc1*^{m1N} mice typically survive to 10.5 weeks [65], and phenotypic onset in *Npc1*^{I1061T} mice occurs at 9-10 weeks; assessments were adjusted accordingly to account for differences in lifespan compared to the *Npc1*^{m1N} model.

Disease phenotype was also evaluated in treated and untreated mice to determine efficacy of gene therapy in slowing progression (Fig 8B). From weeks 9-12 and weeks 12-15, AAV9 treated *Npc1*^{I1061T} mice had significantly lower composite scores compared to saline-injected mice, but scores were still higher than *Npc1*$^{+/+}$ mice ($p < 0.0001$ for all comparisons; two-way ANOVA with mixed effects analysis with Tukey's multiple comparisons test).

Week of peak weight and percent weight change between 10 and 14 weeks were evaluated to assess disease onset and progression. Treated mice reached peak weight significantly later than saline-injected mice (12.9 ± 3.8 weeks vs. 10.9 ± 1.1 weeks; $p = 0.008$, Mann-Whitney test) (Fig 8C). Treated mice gained weight from 10-14 weeks (3.8% ± 6.0%), similar to *Npc1*$^{+/+}$ mice (7.3% ± 2.7%) ($p = 0.37$). In contrast, saline-injected mice lost weight (-12.3% ± 11.0%) and were significantly different from treated ($p = 0.01$) mice (Fig 8D, Kruskal-Wallis test with Dunn's multiple comparisons test). Longitudinal weight data further demonstrates that treated mice survive and maintain weight longer than saline-injected *Npc1*^{I1061T} mice (Fig S1E,F; Table S4C).

AAV9 treatment transduces the cerebellum of *Npc1*^{I1061T} mice but without pathological improvement

ddPCR was used to assess h*NPC1* copy number in the cerebellum of mice at 14-weeks old (age-matched cohort). At 14 weeks, the typical end stage for untreated *Npc1*^{I1061T} mice, treated mice demonstrated increased h*NPC1* copy numbers compared to saline-injected mice ($p = 0.008$, Kruskal-Wallis test with Dunn's multiple comparisons test; Fig 9A). Parallel western blot analysis confirmed similar NPC1 protein presence in treated and saline-injected *Npc1*^{I1061T} mice (NPC1 protein antibody captures both human and mouse NPC1) (Fig 9B, representative blot in Fig S7A,B).

Cerebellar pathology in the age-matched cohort was evaluated using immunofluorescence staining and western blotting. *Npc1*^{I1061T} mice treated with AAV9 showed some survival of Purkinje neurons in anterior lobules of the cerebellum. However, global Purkinje neuron loss across the cerebellum remained comparable between treated and saline-injected mice (Fig 9C). Analysis of Calbindin D protein levels revealed similarly low Calbindin D levels in the cerebellum of treated and saline-injected mice, both of which were lower than healthy *Npc1*$^{+/+}$ mice (Fig 9E, representative blot Fig S7C,D). Microgliosis did not appear reduced in treated mice compared to saline-injected mice, as indicated by IBA1 labeling (Fig 9D).

Similarly, CD68 protein levels, a reactive microglial marker, do not appear reduced in the cerebellum of treated mice (Fig 9F, representative blot Fig S7E,F). Finally, reactive astrocytosis, as measured by GFAP protein levels, is similar in treated mice compared to saline-injected mice (Fig 9G, representative blot Fig S7G,H).

AAV9 treatment of *Npc1*^{I1061T} mice results in successful transduction of cerebrum and liver with reduced hepatic pathology

ddPCR was used to measure h*NPC1* copy number in the cerebrum and liver in the age-matched cohort (14-weeks old) and at humane endpoint/survival. In the age-matched cohort, h*NPC1* copy number in both the cerebrum (Fig 10A) and liver (Fig 10C) were elevated compared to saline-injected mice. In the cerebrum, an increasing h*NPC1* copy number significantly predicted extended lifespan (Fig 10B), whereas in the liver, an increase in h*NPC1* copy number was significantly associated with decreased lifespan (Fig 10D) (linear regression analysis). In the liver of age-matched mice, immunohistochemical staining revealed a partial reduction of CD68+ macrophages compared to saline-injected mice, albeit not to normal *Npc1*$^{+/+}$ levels (Fig 10F; representative images Fig 10E).

Discussion

We examined dose and age at intervention as key factors in optimizing systemically delivered AAV9-EF1a(s)-h*NPC1* gene therapy. Higher doses of AAV9-EF1a(s)-h*NPC1* and treatment during the pre-symptomatic period in the null *Npc1*^{m1N} model significantly improved survival and slowed disease progression compared to lower doses or later treatment. Notably, mice receiving higher doses had the longest survival times, though they did ultimately succumb to NPC1 disease. Additionally, we assessed efficacy of gene therapy in the hypomorphic *Npc1*^{I1061T} mouse, which carries a missense variant, and found that AAV9-EF1a(s)-h*NPC1* successfully increased survival and slowed disease progression in this model.

NPC1 can manifest early and severely, though many individuals experience the first neurological sign in childhood or adolescence, often followed by significant diagnostic delays. Previous gene therapy studies have focused on treatment of neonatal *Npc1*^{m1N} mice [42, 43, 45, 46]. Importantly, we assessed gene therapy efficacy in juvenile mice before and after symptom onset. *Npc1*^{m1N} mice treated pre-symptomatically showed greatest improvements in survival and slowed disease progression. However, mice treated in early disease stage (6 weeks) still exhibited slight survival benefits, indicating the value of early-symptomatic treatment. Establishing a dose- and age-dependent effect is crucial, especially for diseases like NPC1, which are typically diagnosed symptomatically and are not currently part of newborn screening. By demonstrating the benefits of early intervention, our work highlights the need for expanded newborn screening programs, which would enable earlier diagnosis and support treatment of NPC1 individuals before neurological manifestations occur.

Although the *Npc1*^{I1061T} model has not been previously studied, another hypomorphic mouse model (*Npc1*^{nmf164}) which carries a D1005G amino acid substitution, has been examined in gene therapy studies [46]. Both models exhibit late-onset and slower progression compared to *Npc1*^{m1N} mice, which more closely mirrors most human cases. However, the D1005G residue is not conserved in humans and its impact on protein folding or stability is unclear [81]. In contrast, the *Npc1*^{I1061T} model represents a prevalent human variant, with NPC1 p.I1061T encoding a misfolded protein targeted for ERAD [64, 65]. This variant is the most common disease-causing allele in individuals of European descent, accounting for 15-20% of pathological alleles [62, 82, 83]. We demonstrate significant improvement in survival, delayed disease progression, and liver (though not cerebellar) pathology with systemic gene therapy, even in the presence

of residual NPC1 protein. These findings might suggest broader applicability of gene therapy across different patient populations, including those with slower-progressing, later-onset NPC1.

While our high dose showed the most significant survival benefits and improved transduction of multiple organs affected by NPC1, its direct translation to humans requires careful consideration. For comparison, Zolgensma, an FDA-approved therapy for SMA1, is administered at $1.1x10^{14}$ vg/kg, whereas our high dose of $3.06x10^{14}$ vg/kg exceeds that level. Although we did not observe toxicity at this higher dose, clinical experiences with AAV8-mediated gene therapy for X-linked myotubular myopathy underscore potential risks, where 3 of 14 patients experienced fatal liver failure at a dose of $3.5x10^{14}$ vg/kg [84]. These observations highlight the importance of dose escalation studies in preclinical models to refine dosing strategies for translation to human applications. Our medium AAV9 dose of $1.28x10^{14}$ vg/kg – comparable to Zolgensma – showed significant improvements in survival and disease progression, suggesting that doses within this range could balance efficacy and safety. Mice receiving higher doses had the longest survival times, though they ultimately succumbed to disease progression. As necropsies were not carried out, the exact cause of death at the predefined humane endpoint is not known. We hypothesize that because many neurons and cells throughout the CNS remain uncorrected following a single injection of the gene therapy, the disease burden eventually outweighs the capabilities of the transduced, healthy cells. If correct, this theory highlights the importance of widespread transduction, best case scenario being correction of 100% of cells, especially of neurons throughout the CNS. Recognizing this is not yet possible, toxicity must be assessed for high doses aimed at maximizing transduction prior to clinical translation. Together, these findings support the notion that increasing doses achieve greater benefit, the importance of achieving adequate dosing for therapeutic efficacy, and the need to balance efficacy with safety in future studies.

Regarding readout measures of mice in the same dose group, a comparison of weight metrics reveals greater variability in the medium and high dose treatment groups while survival in the medium dose group covers a wide range. Retro-orbital administration, as performed by human hand, is subject to inconsistency. To minimize this potential confounder, a veterinarian with extensive surgical experience in rodent models was the only person to perform RO injections for gene therapy studies from our group to date. Another potential contributor to variability within the different readout measures is weight at time of injection. However, no significant correlation was found between this data metric and the survival, h*NPC1* copy number, or percent weight gain from 6-9 weeks of age. Finally, handling of vector and different vector productions could contribute to variability. To minimize this risk, all vector productions were purchased from University of Pennsylvania Vector Core, now Franklin Biolabs. Vector was thawed only once following dilution and the same vector production batch was used for the high and low dose cohorts. The medium dose cohort/study spanned a greater range of time and provided an internal control as three different batches were used. There was no correlation between the vector batch and lifespan of the mice in the medium dose cohort.

To compare the effects of age of treatment in *Npc1*^{m1N} mice, we used a fixed-analysis point at 9 weeks of age, just before humane endpoint. This age-matched timepoint allowed for consistent comparisons of pathology and vector transduction but did not account for treatment-duration-matched intervals (e.g., assessing all mice at a fixed period, such as 2 weeks post-treatment). Notably, mice treated at 8 weeks exhibited higher h*NPC1* copy numbers in the cerebrum and liver compared to those treated at 4 or 6 weeks. However, it is unclear if this trend would persist in a treatment-duration-matched cohort. Future studies could explore post-treatment intervals to better understand how vector expression changes over time and more directly compare the impact of age of treatment on transduction efficiency.

Additionally, we did not determine which cell types were transduced by AAV9 administration or whether neuronal dysfunction or loss contributed more to pathology. Future studies might assess the transduction of cell types across the brain, investigating both cell death and dysfunction. For instance, we observed Purkinje neuron loss in the cerebellum (a well-described phenomenon [67]), but others have described lipid storage without cell loss in the pyramidal cells of the hippocampus [85, 86]. Understanding which cell types are

most affected and best transduced is essential for clinical success of this gene therapy. Another limitation of this study is the absence of direct quantification of accumulating metabolites in the brain. For example, while the overall cholesterol levels in the brain remain unchanged in NPC1, its intracellular localization is disrupted, leading to pathological effects [8, 87]. To address lipid accumulation, we used mass spectrometry imaging to measure changes in sphingolipids that change in both quantity and distribution. This provided valuable insights into lipid changes in response to treatment, but future studies could incorporate high-performance liquid chromatography to enhance our understanding of lipid storage correction after gene therapy by broadening the analysis of lipid metabolites.

Future studies could also explore combining NPC1 gene therapy with chaperone molecules or substrate reduction therapy, given that gene therapy alone does not entirely halt disease progression. For example, Miglustat, an FDA-designated compound for use in combination with arimoclomol (Miplyffa), reduces glycosphingolipid accumulation but does not address the root cause [10, 88, 89]. Incorporating gene therapy could address this root cause while enhancing therapeutic outcomes by simultaneously reducing disease burden.

In summary, systemic AAV9-EF1a(s)-h*NPC1* delivery significantly impacts NPC1 disease phenotypes and improves survival in both severe and milder disease models, with delivery of high doses and pre-symptomatic treatment providing greatest impact. The findings presented here lay the groundwork for translating this promising therapy to clinical trials for individuals with NPC1 deficiency. Our work has broader implications for gene therapy targeting other lysosomal-membrane spanning proteins, such as those implicated in neuronal ceroid lipofuscinosis [20, 90, 91] and Mucolipidosis type IV [92, 93]. The ability of gene therapy to improve survival and delay disease progression in juvenile mice offers hope for diseases where early detection and intervention remain significant challenges. While gene therapy may not entirely halt disease progression in NPC1, the demonstrated survival benefits emphasize its potential in managing other similar disorders where early, aggressive intervention is critical.

Materials & Methods

Vector construction and production

The vector, AAV9-EF1a(s)-h*NPC1* was previously described and produced by the University of Pennsylvania Vector Core [18].

Animals

All animal work in these studies was carried out in accordance with the National Institutes of Health Animal Care and Use Committee approved protocols. Heterozygous (BALB/cNctr-*Npc1*^{m1N}/J strain; Jackson Laboratory strain # 003092) *Npc1*$^{+/m1N}$ mice were crossed to obtain homozygous mutants (*Npc1*$^{m1N/m1N}$) and wildtype controls (*Npc1*$^{+/+}$). *Npc1*^{I1061T} mice were generated by crossing heterozygous *Npc1*$^{+/I1061T}$ mice (B6.129-*Npc1*^{tm1Dso}/J strain; Jackson Laboratory strain # 027704) to obtain homozygous mutants and *Npc1*$^{+/+}$ controls. We use single allele notation to indicate homozygosity. Mice were weighed weekly and then more frequently as the disease progression neared humane endpoint. Mice were euthanized at a predefined humane endpoint which occurred when at least two of the following four criteria were met: weight falling below 70% of peak weight, repeatedly falling to side during movement, dull eyes or palpebral closure of eyes, or reluctance to move.

As per the ARRIVE Essential 10, the following information refers to the studies contained herein. All studies included saline-injected or untreated mice (*Npc1*^{m1N} or *Npc1*$^{+/+}$, respectively) as control groups. The same control mice from the *Npc1*^{m1N} line were used for the dose and age at injection studies while an appropriate groups of control mice from the *Npc1*^{I1061T} line were used for the corresponding study. A total of 238 mice were used in these studies. Group sample size is stated in the legend or figure for each analysis.

Data for dose and age of treatment study includes all saline-injected and medium-dose AAV9 *Npc1*^{m1N} mice as well as untreated *Npc1*$^{+/+}$ at 4 weeks. No specific exclusion criteria were set a priori, and all mice included in the studies were randomly assigned to treatment or control groups using a blocking method. Except for the researcher overseeing the studies, those involved in vector injections and data acquisition remained blinded to the greatest extent possible. The primary outcome measure was survival. Secondary outcome measures included behavioral assessments, weight, h*NPC1* copy number, and pathology. Details of statistical analyses are found in the results, methods, or figure legends. Experimental animals, procedures, and results are contained with the methods and results of this publication.

Phenotypic Assessment

Mice were tested starting at 6 weeks of age (phenotypic onset) and every three weeks thereafter until humane endpoint or inability to complete the evaluation. The phenotype score evaluates five behaviors associated with the NPC1 phenotype in diseased mice as previously described: hindlimb clasp, motor function, kyphosis, grooming, and a balance-ledge test for cerebellar ataxia [66]. Each phenotype is scored from 0 to 3 with increasing scores representing a more compromised disease state.

Phenotypic testing was carried out in a blinded fashion such that individual mice within a cage had distinct tail markings. Evaluators had access only to cage card numbers and tail markings to identify mice. The order in which mice were tested varied for each testing date. All animals were group housed.

Administration of vector

Treated *Npc1*^{m1N} mice received a retro-orbital injection of AAV9-EF1a(s)-h*NPC1* at 4 weeks (weaning), 6 weeks, or 8 weeks of age. *Npc1*^{I1061T} mice received a retro-orbital injection of AAV9-EF1a(s)-h*NPC1* at 4 weeks old. Control littermate *Npc1*^{m1N} or *Npc1*^{I1061T} mice received a retro-orbital injection of 0.9% saline at 4 weeks or the specified age. Mice were anesthetized using isoflurane for 30-60s and then injected retro-orbitally with a 30-gauge needle affixed to a 0.3 cc syringe. Some control *Npc1*$^{+/+}$ mice received retro-orbital injections of saline while others remained un-injected.

Dose Selection

Our original dose for mice treated at 4 weeks was $1.2x10^{12}$ vector genomes (vg) per mouse (mean: $1.28x10^{14}$ vg/kg), based on our previously published data [18, 44]. This served as the medium dose and the comparator across studies. For ease of comparison to other animal and clinical studies, doses are provided as vector genomes/kg.

For dose comparison, doses were selected and scaled based on vector genomes/mouse. We used a low dose of $1x10^{11}$ vg/mouse ($7.87x10^{12}$ vg/kg), representing a 1-log reduction from the baseline. The high dose, $4.3x10^{12}$ vg/mouse ($3.06x10^{14}$ vg/kg), was dictated by the maximum concentration achievable through the University of Pennsylvania Vector Core, now Franklin Biolabs, and volume constraints allowed by the Animal Care and Use Committee. For the age of treatment study, dose was calculated per weight to deliver $1.28x10^{14}$ vg/kg for each mouse at either 6 or 8 weeks of age.

Tissue collection and homogenization

Mice were anesthetized with an intraperitoneal injection of Avertin (lethal dose of 0.04 mL/gm) for euthanasia as previously described [44]. When mice were insensate, the chest cavity was opened, and mice were perfused with 0.9% saline. Immediately, half of the brain, one lobe of the liver, and a piece of spleen, kidney, lung, and leg muscle were collected and frozen on dry ice for tissue homogenization. Mice were then perfused again with 4% paraformaldehyde to fix tissues; remaining organs (half of the brain, liver) were collected and stored post-fixation in 4% PFA overnight and then rinsed and stored in phosphate-buffered-saline (PBS).

A Benchmark Scientific Beadbug homogenizer was used to homogenize frozen tissue with UltraPure water. Tissue was placed in tubes with 3 mm zirconium beads (cerebrum, cerebellum, brainstem, liver, spleen, leg muscle) or 1.5 mm zirconium beads (kidney, lung) and homogenized 3 times for 30 seconds at speed 400. Resulting homogenate was aliquoted into tubes for DNA extraction and protein analysis, the latter of which also had RIPA buffer with proteinase inhibitor cocktail (11 836 170 001; Millipore Sigma, Burlington, MA) [44].

Western blotting

Protein levels from cerebrum, cerebellum, and liver homogenates were quantified using a BCA Assay (23225, Thermo Fisher Scientific, Waltham, MA). Equal amounts of protein (50 ug for liver, cerebellum, and cerebrum) were run on 4-12% Bis-Tris SDS-polyacrylamide gels (NP0321BOX/Invitrogen by Thermo Fisher Scientific) and separation was achieved via electrophoresis; protein was then transferred to a nitrocellulose membrane (Life Technologies) and blocked for 1 hour in 5% milk in 0.01% PBSTween. Samples were washed in 0.01% PBSTween incubated overnight at 4 °C on a rocking platform with primary antibody (Table S1). Blots were washed three times and incubated with secondary antibodies for 1 hour at room temperature (Table S1), then washed again. Bands were imaged using the LI-COR Odyssey® CLx Imaging System.

Histology

Brain and liver tissue from each group were acquired at 9 or 10 weeks of age (*Npc1*^{m1N}), 14 weeks of age (*Npc1*^{I1061T}), or humane endpoint (both models). Post-fixation tissues were embedded in agarose blocks (3.5% agarose, 8% sucrose, PBS) and sectioned parasagittaly (30 µm) using a Leica VT1200 S vibratome. Free-floating sections were collected, incubated in 1.6% H_2O_2 in PBS, then washed in 0.25% Triton X-100/PBS (PBSt). After blocking for 1 hour at room temperature in PBSt/normal goat serum, samples were incubated in primary antibodies overnight at 4°C (Table S1). Samples were washed in PBSt and then incubated with secondary antibodies for 1 hour at room temperature (AlexaFluor 488 or 594; Table S1). Filipin staining (Sigma-Aldrich, F9765) was finally performed to allow visualization of unesterified cholesterol accumulation (0.05mg/mL) with a 20-minute incubation. ProLong Gold mounting medium alone (Thermo Fisher Scientific, P36934) or with DAPI (Thermo Fisher Scientific, P36935) was used to coverslip after mounting tissue sections to slides.

For immunohistochemical staining after primary antibody incubation, slides were incubated in biotinylated secondary antibody and washed in PBSt. A biotinylated horse radish peroxidase was preincubated with avidin to form Avidin-Biotin Complex (ABC; Vector Laboratories SK-4100) and the tissues were incubated in ABC (in PBS) for 1 hour. Tissues were then washed in PBS and incubated for 10 minutes in a 3,3'-Diaminobenzidine (DAB; Vector Laboratories PK-4000) solution before mounting and cover slipping with VectaMount (Vector Laboratories, H-5700).

Histoserv, Inc. (Germantown, MD) performed paraffin embedding (formalin fixed, paraffin embedded i.e., FFPE, tissues). For immunofluorescent staining, FFPE sections (3 um) were collected and underwent antigen retrieval in a citrate (pH 6.0, Electron Microscopy Sciences, 62706-10) or Tris-EDTA (pH 9.0, Abcam, AB93684) buffer. Slides were then incubated in primary antibody diluted in antibody diluent with BSA and preservative (Thermo Fisher Scientific, 003218) at 37°C for 1 hour, washed in PBS, and incubated in secondary antibodies for 30 minutes at 37°C (Table S1). Tissues were then coverslipped with ProLong Gold mounting medium with DAPI.

Image capture and analysis

Fluorescent imaging was performed with an inverted Zeiss AxioScan Z1slide scanner with Zen Blue 3.8 as previously described in [44]. Brightfield images were captured on the same Zeiss AxioScan Z1 slide scanner. Adobe Photoshop 2023 (v.23.5.0) and 2024 (v.25.1.0) was used to modify all images in a figure/group identically by resizing and adjusting brightness and/or contrast.

Quantification of CD68 area

Percent of positive CD68 area relative to total area in liver sections was determined according to methods previously described [94] using Image-Pro. V11 software (Media Cybernetics, Inc.). Images were processed using ten regions of interest with total area 900,000 μm^2 to determine average percent positive area.

Copy number analysis by ddPCR

Vector copy number was measured by droplet digital PCR (ddPCR) as previously described with h*NPC1* and *GAPDH* primers (Bio-Rad; [44]). 0.5-50 ng of DNA was used for gene copy number quantification with brain (cerebrum, cerebellum, or brainstem) and liver homogenates. Additional organs including spleen, kidney, lung, and leg muscle were assayed for the 10-week-old cohort in the dose study, using 0.5-5 ng of DNA per reaction. Signals for droplets were either positive or negative for h*NPC1* and/or *GAPDH* as determined using BioRad's QuantaSoft version 1.7.4.0917 software.

Mass spectrometry imaging and lipidomics

The fresh frozen half of the brain was sectioned on a CryoStar NX50 Cryostat set to -12°C in preparation for mass spectrometry imaging. The frozen tissue was divided into 4-6 10 µm thick sections, which were then promptly thaw-mounted onto ITO slides (MIDSCI) and stored at -80°C. Immediately prior to imaging sections, the slides were removed from the -80°C freezer and washed with ice cold 50 mM ammonium formate for 20 seconds then dried in vacuo. 9-aminoacridine and 2,5-dihydroxybenzoic acid were chosen as the matrices for negative and positive mode respectively. One hundred milligrams of solid matrix was dissolved in 10 mL of 50:50 H_2O:ACN + 0.2% TFA and filtered using a 0.2 µm syringe filter. Filtered matrix was applied to the slide using the HTX TM Sprayer.

Mass spectrometry imaging was performed on a Bruker RapifleX MALDI TOF with a 10 kHz laser set to 60% power, 500 laser shots per pixel, and a step size of 35 µm. The instrument was operated in negative and positive mode within an m/z range of 200-1800. All data processing including region-of-interest determination, spatial segmentation, mass spectra extraction and image generation were performed using Bruker's Scils software. LIPID MAPS and the Human Metabolome Database were used to annotate and identify lipids according to accurate mass measurements. Hedges-g analysis was performed for GM2 lipid species across the experimental groups using total ion count normalized peak areas.

Statistical analysis

Randomization was achieved with multiple cohorts. Mice within each cohort were included from each age at injection group or at each dosage. Statistical analysis was performed using GraphPad Prism version 9.5.1 for Windows or Mac. Normality was evaluated for data sets and appropriate parametric or nonparametric tests were selected for further analysis. Data is presented as mean ± SD. Kaplan Meier survival curves used Log-Rank Mantel-Cox test to assess significance, with a Bonferroni-correction applied for $P<0.0083$ for multiple (six) comparisons. Other statistical tests were as follows: Kruskal-Wallis test with Dunn's multiple comparison's test, one-way ANOVA with Tukey's multiple comparisons test, two-way ANOVA with Tukey's multiple comparisons test, linear regression test (all multiple comparisons test use post hoc Bonferroni's correction). In all figures: * $p < 0.05$, ** $p < 0.01$, *** $p < 0.001$, **** $p < 0.0001$.

Acknowledgments:

We thank Laura L. Baxter for her support and instruction in statistical analysis as well as Stephen Wincovitch for imaging and quantification support. We are grateful for the technical assistance in digital droplet PCR provided by the National Cancer Institute Genomics Core. We sincerely acknowledge the NIH animal care and veterinary staff for the care of mice used in these studies. We also recognize the driving

force behind this work: individuals with NPC1 disease. Their perseverance in the face of this debilitating disease inspires and humbles us.

Funding

This work was supported by the Intramural Research Program of the National Human Genome Research Institute (NHGRI) at the NIH (1ZIAHG000068-16), the *Eunice Kennedy Schriver* National Institute of Child Health and Human Development (NICHD) at the NIH (ZIAHD008988), grants from the NIH (R01NS114413, R01NS124784), and the Ara Parseghian Medical Research Fund at the University of Notre Dame. AVM, ALG, TG, CDD, AI, CPV, and WJP were supported by the Intramural Research Program at NHGRI; CDD, KM, SRG, FDP were supported by the Intramural Research Program at NICHD. Additional support for CDD came from the Support Of Accelerated Research for NPC (Hide & Seek Foundation and Dana's Angels Research Trust). DP-J was supported by the Bridge to Doctoral Program and the Diversifying Faculty in Illinois Fellowship.

Conflict of Interest Statement

CPV and WJP have NIH patents filed on work related to NPC1 genes and the AAV gene therapy treatment of NPC1 (US Patent Publication Numbers 20180104289, 20210113635).

Figure 1: *Npc1*^{m1N} mice treated with AAV9-EF1a(s)-h*NPC1* vector show increased survival and delayed disease phenotype progression.
(A) Kaplan-Meier survival curve of mice treated with low, medium, and high dose AAV9 and saline injected mice (results presented in Table S2A) (saline n = 15, low n = 10, medium n = 24, high n =8). **(B)** Composite phenotype scores for each dosage group with measurements taken every 3 weeks, starting at 6 weeks (results presented in Table S3A) (saline n = 14, low n = 10, medium n = 13, high n = 8, *Npc1*$^{+/+}$ n = 21). **(C)** Week at which mice reached peak weight (Kruskal-Wallis with Dunn's multiple comparisons test). **(D)** Percent weight change between 6 and 9 weeks old (One-way ANOVA with Tukey's multiple comparisons test). For (C, D): saline n =15, low n = 10, medium n = 24, high n = 8; for (D): *Npc1*$^{+/+}$ n = 21. For all: * $p < 0.05$, ** $p < 0.01$, *** $p < 0.001$, **** $p < 0.0001$. Data presented as mean ± SD for B, C, D.

Figure 2: Higher dose of AAV9 enhance viral transduction in brain and liver of *Npc1*^{m1N} mice.
(A, B, C) Analysis of cerebellum (A), cerebrum (B), and liver (C). **(Ai, Bi, Ci)** h*NPC1* copy number in cerebellum (Ai), cerebrum (Bi), and liver (Ci) from 10-week-old mice (Kruskal-Wallis test with Dunn's multiple comparisons test). For Ai, Bi, Ci: (saline n = 6, low n = 5, medium n = 6, high n = 6, *Npc1*$^{+/+}$ n = 9). **(Aii, Bii, Cii)** NPC1 protein levels were assessed via western blot in 10-week-old mice to confirm amount of NPC1 protein in the cerebellum (Aii), cerebrum (Bii) and liver (Cii) (Kruskal-Wallis test with Dunn's multiple comparisons test). For Aii (saline n = 6, low n = 5, medium n = 6, high n = 6, *Npc1*$^{+/+}$ n = 8). For Bii, Cii (saline n = 6, low n = 5, medium n = 6, high n = 6, *Npc1*$^{+/+}$ n = 7). **(Aiii, Biii, Ciii)** Linear regression of h*NPC1* copy number in the cerebellum (Aii), cerebrum (Bii) and liver (Cii) in end stage mice. For Aiii, Biii (saline n = 14, low n = 9, medium n = 20, high n = 6, *Npc1*$^{+/+}$ n = 17). For Ciii (saline n = 14, low n = 9, medium n = 18, high n = 5, *Npc1*$^{+/+}$ n = 17). For all: * $p < 0.05$, ** $p < 0.01$, *** $p < 0.001$, **** $p < 0.0001$. Data presented as mean ± SD for Ai, Bi, Ci, Aii, Bii, Cii.

Figure 3: Dose-dependent amelioration of cerebellar pathology in 10-week-old *Npc1*^{m1N} mice.
(A) Representative immunofluorescence staining in free floating sections for: unesterified cholesterol storage (top row), reactive astrocytes and Bergmann glia (middle row), and Purkinje neurons (bottom row). Insets are of anterior lobules (IV/V). **(B)** Representative immunofluorescence staining in formalin-fixed, paraffin embedded sections for microgliosis. Insets are of posterior lobules (lobule IX). For (A, B) Scale bar = 1000 microns for panels, 250 microns for insets. **(C, D, E)** Protein levels for GFAP (C), Calbindin (D), CD68 (E), were assessed via western blot for 10-week-old mice (Kruskal-Wallis test with Dunn's multiple comparisons test) (saline n = 5, low n = 5, medium n = 6, high n = 5, *Npc1*$^{+/+}$ n = 5). For C, D, E: * $p < 0.05$, ** $p < 0.01$, *** $p < 0.001$, **** $p < 0.0001$, data presented as mean ± SD.

Figure 4: Dose-dependent reduction of liver pathology in 10-week-old *Npc1*^{m1N} mice.
(A) Representative CD68+ immunohistochemical staining of macrophages (free floating sections). Scale bar = 250 microns. **(B)** Quantification of percent area CD68 labelled in 10-week-old mice (Kruskal-Wallis test with Dunn's multiple comparisons test) (saline n = 5, low n = 5, medium n = 6, high n = 6, *Npc1*$^{+/+}$ n = 9). **(C)** Representative cholesterol storage (filipin labeling) and CD68+ immunofluorescent staining in the liver (free floating sections). Yellow arrows in high-dose inset denote groups of cells without cholesterol storage. Scale bar for panel (A) = 500 microns, scale bar for (C) = 100 microns. For B: * $p < 0.05$, ** $p < 0.01$, *** $p < 0.001$, **** $p < 0.0001$, data presented as mean ± SD.

Figure 5: AAV9 treatment at 4-weeks improves survival and delays disease progression in *Npc1*^{m1N} compared to treatment at 6- or 8- weeks of age.
(A) Kaplan-Meier survival curve of mice treated with AAV9 (results presented in Table S2B). **(B)** Composite phenotype scores for each dosage group with measurements taken every 3 weeks, starting at 6 weeks (results presented in Table S3B) (saline n = 14, 4 weeks n = 13, 6 weeks n = 20, 8 weeks n = 20, *Npc1*$^{+/+}$ n = 21). **(C)** Week at which mice reached peak weight (Kruskal-Wallis test with Dunn's multiple

comparisons test). **(D)** Percent weight change between 6 and 9 weeks old (One-way ANOVA with Tukey's multiple comparisons test). For C, D (saline n = 15, 4-week n = 24, 6-week n = 20, 8-week n = 20) for D (*Npc1*$^{+/+}$ n = 21). For all: * p < 0.05, ** p < 0.01, *** p < 0.001, **** p < 0.0001. Data presented as mean ± SD for B, C, D.

Figure 6: Age of treatment affects AAV9 transduction in cerebellum and treatment at 4 weeks reduces cerebellar pathology.

(A) ddPCR was used to measure h*NPC1* copy number in the cerebellum of mice at 9 weeks old (Kruskal-Wallis test with Dunn's multiple comparisons test) (saline n = 6, 4 weeks n = 6, 6 weeks n = 4, 8 weeks n = 4, *Npc1*$^{+/+}$ n = 4). **(B)** NPC1 protein levels were assessed via western blot in 9-week-old mice to confirm amount of NPC1 protein in the cerebellum (Kruskal-Wallis test with Dunn's multiple comparisons test) (saline n = 3, 4-week n = 6, 6-week n = 4, 8-week n = 4, *Npc1*$^{+/+}$ n = 4). **(C)** Representative immunofluorescence staining in free floating section for Purkinje neurons, insets are of anterior lobules (IV/V). **(D)** Representative immunofluorescence staining in formalin-fixed, paraffin embedded sections for microgliosis. Insets are of posterior lobules (lobule IX). For C,D: scale bar = 1000 microns for panels, 250 microns for insets. **(E, F, G)** Protein levels for Calbindin (E), CD68 (F), GFAP (G) were assessed via western blot for each 9-week-old mice cohort (Kruskal-Wallis test with Dunn's multiple comparisons test) (saline n = 3, 4 weeks n = 3, 6 weeks n = 4, 8 weeks n = 4, *Npc1*$^{+/+}$ n = 4). For all: * p < 0.05, ** p < 0.01, *** p < 0.001, **** p < 0.0001. Data presented as mean ± SD for A, B, E, F, G.

Figure 7: Age of treatment impacts AAV9 transduction in cerebrum and liver and hepatic pathology.

(A, C) ddPCR was used to measure h*NPC1* copy number in mice at 9-weeks old in cerebrum (**A**) and liver (**C**) (Kruskal-Wallis test with Dunn's multiple comparisons test). For A: (saline n = 6, 4 weeks n = 3, 6 weeks n = 4, 8 weeks n = 4, *Npc1*$^{+/+}$ n = 4), for C: (saline n = 6, 4 weeks n = 4, 6 weeks n = 4, 8 weeks n = 4, *Npc1*$^{+/+}$ n = 4). **(B, D)** Linear regression of h*NPC1* copy number in end stage mice in cerebrum (**B)** and liver **(D)**. For B: (saline n = 14, 4 weeks n = 19, 6 weeks n = 20, 8 weeks n = 20, *Npc1*$^{+/+}$ n = 17), for D: (saline n = 14, 4 weeks n = 18, 6 weeks n = 20, 8 weeks n = 20, *Npc1*$^{+/+}$ n = 17). **(E)** Representative immunohistochemical staining of macrophages in the liver in 9-week-old mice (free-floating sections). Scale bar = 250 microns. **(F)** Quantification of percent area CD68 labelled in 9-week-old mice (Kruskal-Wallis test with Dunn's multiple comparisons test) (saline n = 6, 4 weeks n = 8, 6 weeks n = 4, 8 weeks n = 4, *Npc1*$^{+/+}$ n = 4). For all: * p < 0.05, ** p < 0.01, *** p < 0.001, **** p < 0.0001. Data presented as mean ± SD for A, C, F.

Figure 8: *Npc1*^{I1061T} mice treated with AAV9 show increased lifespan and delayed disease progression.

(A) Kaplan Meier curve depicts survival of saline injected *Npc1*^{I1061T} mice and *Npc1*^{I1061T} mice treated with AAV9 at 4 weeks. **(B)** Composite phenotype score for each group was measured from 6 to 21 weeks of age at 3-week intervals. **(C)** Week mice reached peak weight (Mann-Whitney test). **(D)** Percent weight change from 10 to 14 weeks (Kruskal-Wallis with Dunn's multiple comparisons). For A, B, C, D (saline n = 11, treated n = 15) and for B,D (*Npc1*$^{+/+}$ n = 15). For all: * p < 0.05, ** p < 0.01, *** p < 0.001, **** p < 0.0001. For B, C, D: data presented as mean ± SD.

Figure 9: AAV9 treatment effectively transduces the cerebellum of *Npc1*^{I1061T} mice, modestly impacts cerebellar pathology.

(A) ddPCR was used to measure h*NPC1* copy number in the cerebellum in mice at 14-weeks old (Kruskal-Wallis test with Dunn's multiple comparisons test) (saline n = 4, AAV9 n = 5, *Npc1*$^{+/+}$ n = 4). **(B)** NPC1 protein levels were assessed via western blot in 14-week-old mice to determine amount of NPC1 protein in the cerebellum (Kruskal-Wallis test with Dunn's multiple comparisons test) (saline n = 4, AAV9 n = 5, *Npc1*$^{+/+}$ n = 5). **(C)** Representative immunofluorescence staining in free floating section for Purkinje neurons, insets are of anterior lobules (IV/V). **(D)** Representative immunofluorescence staining in formalin-fixed, paraffin embedded sections for microgliosis. Insets are of posterior lobules (lobule IX). For C,D:

scale bar = 1000 microns for panels, 250 microns for insets. **(E, F, G)** Protein levels for Calbindin (E), CD68 (F), GFAP (G) were assessed via western blot for each 9-week-old mice cohort (Kruskal-Wallis test with Dunn's multiple comparisons test) (saline n = 4, AAV9 n = 5, *Npc1*$^{+/+}$ n = 5). For all: * $p < 0.05$, ** $p < 0.01$, *** $p < 0.001$, **** $p < 0.0001$. Data presented as mean ± SD for A, B, E, F, G.

Figure 10: Transduction efficacy of AAV9 in *Npc1*^{I1061T} mice cerebrum and liver tissue and hepatic pathology.

(**A, C**) ddPCR was used to measure h*NPC1* copy number at 14 weeks in cerebrum (**A**) and liver (**C**). For A,C: (Kruskal-Wallis test with Dunn's multiple comparisons test) (saline n = 4, treated n = 5, *Npc1*$^{+/+}$ n = 5). (**B, D**) Linear regression of h*NPC1* copy number and lifespan in cerebrum (**B**) or liver (**D**). For B: (saline n = 11, treated n = 12, *Npc1*$^{+/+}$ n = 14), D: (saline n = 11, treated n = 13, *Npc1*$^{+/+}$ n = 14). **(E)** Representative immunohistochemical staining of macrophages in liver of saline-injected, treated, and *Npc1*$^{+/+}$ mice at 14 weeks (free floating sections). Scale bar = 250 microns. (**F**) Quantification of percent area CD68 labelled in 14-week-old mice (Kruskal-Wallis test with Dunn's multiple comparisons test) (saline n = 5, treated n = 5, *Npc1*$^{+/+}$ n = 6). For all: * $p < 0.05$, ** $p < 0.01$, *** $p < 0.001$, **** $p < 0.0001$. For A, C, F: data presented as mean ± SD.

SUPPLEMENTAL

Table S1: Antibodies used for immunohistochemical and immunofluorescence staining along with manufacturer and dilution information.

Table S2: Median survival of *Npc1*^{m1N} mice treated with AAV9. Table of median survival for each dose treatment group **(A,** analysis of Fig 1A**)** and each age of treatment group **(B,** analysis of Fig 5A**).** Level of significance is p = 0.0083 based on Bonferroni's correction with 6 comparisons.

Table S3: *Npc1*^{m1N} mice treated with AAV9 vector and *Npc1*$^{+/+}$ mice phenotype score comparison from 6-12 weeks. Two-way ANOVA with mixed effects analysis and Tukey's multiple comparisons test of various dose treatment groups (**A**) and various age treatment groups (**B**) from 6-9 weeks, and 9-12 weeks. Level of significance is p = 0.0083 based on Bonferroni's correction with 6 comparisons.

Table S4: Total sample size for weight curves of each sub study. (**A**) Sample size for male and female mice per treatment group included in dosing study. (**B**) Sample size for male and female mice per treatment group included in age at injection study. (**C**) Sample size for male and female mice per treatment group included in the hypomorphic I1061T study.

S1: Mouse weights. *Npc1*^{m1N} mice treated with AAV9 vector and *Npc1*$^{+/+}$ mice weights over lifespan. Weights are presented as mean ± SD. For the dose study, **(A)** males, **(B)** females. For age at injection: **(C)** males, **(D)** females. For *Npc1*^{I1061T} mice: **(E)** males, **(F)** females. (n) listed in Table S4.

S2: h*NPC1* copy number in tissues of 10-week-old mice treated with varying doses. Gene copy numbers were measured for various organs at 10-weeks-old for *Npc1*^{m1N} mice treated with saline or AAV9 vector at low, medium, and high doses, and untreated *Npc1*$^{+/+}$ mice. Data presented as mean ± SD.

S3: Representative western blots: quantification of NPC1 in cerebrum and liver of *Npc1*^{m1N} mice in dose study.
Representative western blots for quantification of NPC1 in cerebellum **(A)**, quantification shown in Fig 2Aii. Source images for cerebellum **(B)**, right half of blot enlarged in (A). Representative blots for quantification of NPC1 in cerebrum **(C)**, quantification shown in Fig 2Bii. Source images for cerebrum **(D)**, left half of blot enlarged in (C). Representative western blots for quantification of NPC1 in liver **(E)**, quantification shown in Fig 2Cii. Source image for liver **(F)**, right half of blot enlarged in (E). Red box and triangle denote immunoreactive NPC1 protein (~180kDa), black triangle indicates Beta-actin (42kDa). h*NPC1* copy number provided for each sample below (A, C, E). For (D), molecular weight markers are faint in this representative blot; approximate molecular weights were determined from a parallel blot.

S4. Representative western blots: quantification of GFAP, CD68, and Calbindin D in cerebellum of *Npc1*^{m1N} mice in dose study.
Representative western blot for quantification of GFAP **(A)** and CD68 **(C)**, quantification shown in Fig 3C. Source image for GFAP and CD68 **(B)**, right half of blot enlarged in (A, GFAP and C, CD68). Representative western blot for quantification of Calbindin D **(D)**, quantification shown in Fig 3D. Source image for Calbindin D **(E)**, left half of blot enlarged in (D). Brown box and triangle denote GFAP protein (50kDa), purple box and triangle denote CD68 protein (~100 kDa), yellow triangle denotes Calbindin D (28kDa), and black triangle indicates Beta-actin (42kDa). h*NPC1* copy number provided for each sample below blots.

S5: AAV9 modulates sphingolipid accumulation in the brains of *Npc1*^{m1N} mice.
(A) Mass spectrometry imaging of brain of 10-week-old mice treated with varying doses of AAV9. Lipids displayed include **i)** Ganglioside GM2 (d18:1/18:0), **ii)** Hexosylceramide HexCer 46:4;O3, and **iii)**

Dihydroceramide Cer 32:2;O3 (for all groups, n = 3, 4-6 sections assessed). **(B)** Quantification of total ion count (TIC) normalized peak areas for GM2 in cerebellum of 10-week-old mice (Kruskal-Wallis test with Dunn's multiple comparisons test).

S6: Representative western blots: quantification of NPC1, Calbindin D, CD68, and GFAP in cerebellum in *Npc1*^{m1N} mice in age of treatment study.

Representative western blot for quantification of NPC1 and Calbindin D **(A)**, quantification shown in Fig 6B,E respectively. Source image for NPC1, Calbindin D, and Beta-actin **(B)**, left half of blot enlarged in (A). Representative blot for quantification of CD68 and GFAP **(C)**, quantification shown in Fig 6F,G respectively. Source image for CD68 and GFAP **(D)**, left half of blot enlarged in (C). Red box and triangle denote NPC1 protein (~180kDa), yellow triangle denotes Calbindin D (28kDa), purple box and triangle denote CD68 protein (~100kDa), brown box and triangle denote GFAP protein (50kDa), and black triangle indicates Beta-actin (42kDa). h*NPC1* copy number provided for each sample below blots for A, C.

S7: Representative western blots: quantification of NPC1, Calbindin D, CD68, and GFAP in cerebellum in *Npc1*^{I1061T} mice.

Representative western blot for quantification of NPC1 **(A)** and Calbindin D **(C)**, quantification shown in Fig 9B,E respectively. Source image for NPC1 and Calbindin D **(B)**, left third of blot enlarged in (A, NPC1 and C, Calbindin D). Representative blot for quantification of CD68 and GFAP **(D)**, quantification shown in Fig 9F,G respectively. Source image for CD68 and GFAP **(E)**, left third of blot enlarged in (D). Red box and triangle denote NPC1 protein (~180kDa), yellow triangle denotes Calbindin D (28kDa), purple box and triangle denote CD68 protein (~100 kDa), brown box and triangle denote GFAP protein (50kDa), and black triangle indicates Beta-actin (42kDa). h*NPC1* copy number provided for each sample below blots for A, C, D.

REFERENCES

1. Vanier, M.T., *Niemann-Pick diseases.* Handb Clin Neurol, 2013. **113**: p. 1717-21.
2. Ory, D.S., *Niemann-Pick type C: a disorder of cellular cholesterol trafficking.* Biochim Biophys Acta, 2000. **1529**(1-3): p. 331-9.
3. Sleat, D.E., et al., *Genetic evidence for nonredundant functional cooperativity between NPC1 and NPC2 in lipid transport.* Proc Natl Acad Sci U S A, 2004. **101**(16): p. 5886-91.
4. Infante, R.E., et al., *Purified NPC1 protein. I. Binding of cholesterol and oxysterols to a 1278-amino acid membrane protein.* J Biol Chem, 2008. **283**(2): p. 1052-63.
5. Vanier, M.T., et al., *Genetic heterogeneity in Niemann-Pick C disease: a study using somatic cell hybridization and linkage analysis.* Am J Hum Genet, 1996. **58**(1): p. 118-25.
6. Cologna, S.M. and A. Rosenhouse-Dantsker, *Insights into the Molecular Mechanisms of Cholesterol Binding to the NPC1 and NPC2 Proteins.* Adv Exp Med Biol, 2019. **1135**: p. 139-160.
7. Walkley, S.U. and K. Suzuki, *Consequences of NPC1 and NPC2 loss of function in mammalian neurons.* Biochim Biophys Acta, 2004. **1685**(1-3): p. 48-62.
8. Vanier, M.T., *Niemann-Pick disease type C.* Orphanet J Rare Dis, 2010. **5**: p. 16.
9. Patterson, M.C., et al., *Recommendations for the diagnosis and management of Niemann-Pick disease type C: an update.* Mol Genet Metab, 2012. **106**(3): p. 330-44.
10. Mullard, A., *FDA approves first two drugs for rare Niemann-Pick disease.* Nat Rev Drug Discov, 2024.
11. Fields, T., et al., *N-acetyl-L-leucine for Niemann-Pick type C: a multinational double-blind randomized placebo-controlled crossover study.* Trials, 2023. **24**(1): p. 361.
12. Mengel, E., et al., *Efficacy and safety of arimoclomol in Niemann-Pick disease type C: Results from a double-blind, randomised, placebo-controlled, multinational phase 2/3 trial of a novel treatment.* J Inherit Metab Dis, 2021. **44**(6): p. 1463-1480.
13. Patterson, M.C., et al., *Miglustat for treatment of Niemann-Pick C disease: a randomised controlled study.* Lancet Neurol, 2007. **6**(9): p. 765-72.
14. Ory, D.S., et al., *Intrathecal 2-hydroxypropyl-beta-cyclodextrin decreases neurological disease progression in Niemann-Pick disease, type C1: a non-randomised, open-label, phase 1-2 trial.* Lancet, 2017. **390**(10104): p. 1758-1768.
15. Administration, U.S.F.a.D. *FDA approves first treatment for Niemann-Pick disease type C*. 2024 September 25, 2024]; Available from: https://www.fda.gov/news-events/press-announcements/fda-approves-first-treatment-niemann-pick-disease-type-c.
16. Patterson, M.C., et al., *Stable or improved neurological manifestations during miglustat therapy in patients from the international disease registry for Niemann-Pick disease type C: an observational cohort study.* Orphanet J Rare Dis, 2015. **10**: p. 65.
17. Solomon, B.I., et al., *Association of Miglustat With Swallowing Outcomes in Niemann-Pick Disease, Type C1.* JAMA Neurol, 2020. **77**(12): p. 1564-1568.
18. Chandler, R.J., et al., *Systemic AAV9 gene therapy improves the lifespan of mice with Niemann-Pick disease, type C1.* Hum Mol Genet, 2017. **26**(1): p. 52-64.
19. Cain, J.T., et al., *Gene Therapy Corrects Brain and Behavioral Pathologies in CLN6-Batten Disease.* Mol Ther, 2019. **27**(10): p. 1836-1847.

20. Bosch, M.E., et al., *Self-Complementary AAV9 Gene Delivery Partially Corrects Pathology Associated with Juvenile Neuronal Ceroid Lipofuscinosis (CLN3).* J Neurosci, 2016. **36**(37): p. 9669-82.
21. Sondhi, D., et al., *Slowing late infantile Batten disease by direct brain parenchymal administration of a rh.10 adeno-associated virus expressing CLN2.* Sci Transl Med, 2020. **12**(572).
22. Hudry, E. and L.H. Vandenberghe, *Therapeutic AAV Gene Transfer to the Nervous System: A Clinical Reality.* Neuron, 2019. **102**(1): p. 263.
23. Bradbury, A.M., et al., *Krabbe disease successfully treated via monotherapy of intrathecal gene therapy.* J Clin Invest, 2020. **130**(9): p. 4906-4920.
24. Mendell, J.R., et al., *Single-Dose Gene-Replacement Therapy for Spinal Muscular Atrophy.* N Engl J Med, 2017. **377**(18): p. 1713-1722.
25. Al-Zaidy, S., et al., *Health outcomes in spinal muscular atrophy type 1 following AVXS-101 gene replacement therapy.* Pediatr Pulmonol, 2019. **54**(2): p. 179-185.
26. Lowes, L.P., et al., *Impact of Age and Motor Function in a Phase 1/2A Study of Infants With SMA Type 1 Receiving Single-Dose Gene Replacement Therapy.* Pediatr Neurol, 2019. **98**: p. 39-45.
27. Gao, J., R.M. Hussain, and C.Y. Weng, *Voretigene Neparvovec in Retinal Diseases: A Review of the Current Clinical Evidence.* Clin Ophthalmol, 2020. **14**: p. 3855-3869.
28. Russell, S., et al., *Efficacy and safety of voretigene neparvovec (AAV2-hRPE65v2) in patients with RPE65-mediated inherited retinal dystrophy: a randomised, controlled, open-label, phase 3 trial.* Lancet, 2017. **390**(10097): p. 849-860.
29. Tai, C.H., et al., *Long-term efficacy and safety of eladocagene exuparvovec in patients with AADC deficiency.* Mol Ther, 2022. **30**(2): p. 509-518.
30. Manfredsson, F.P., A.C. Rising, and R.J. Mandel, *AAV9: a potential blood-brain barrier buster.* Mol Ther, 2009. **17**(3): p. 403-5.
31. Foust, K.D., et al., *Intravascular AAV9 preferentially targets neonatal neurons and adult astrocytes.* Nat Biotechnol, 2009. **27**(1): p. 59-65.
32. Lykken, E.A., et al., *Recent progress and considerations for AAV gene therapies targeting the central nervous system.* J Neurodev Disord, 2018. **10**(1): p. 16.
33. Duque, S., et al., *Intravenous administration of self-complementary AAV9 enables transgene delivery to adult motor neurons.* Mol Ther, 2009. **17**(7): p. 1187-96.
34. Gray, S.J., et al., *Preclinical differences of intravascular AAV9 delivery to neurons and glia: a comparative study of adult mice and nonhuman primates.* Mol Ther, 2011. **19**(6): p. 1058-69.
35. Bagel, J.H., et al., *Electrodiagnostic testing and histopathologic changes confirm peripheral nervous system myelin abnormalities in the feline model of niemann-pick disease type C.* J Neuropathol Exp Neurol, 2013. **72**(3): p. 256-62.
36. Zincarelli, C., et al., *Analysis of AAV serotypes 1-9 mediated gene expression and tropism in mice after systemic injection.* Mol Ther, 2008. **16**(6): p. 1073-80.
37. Inagaki, K., et al., *Robust systemic transduction with AAV9 vectors in mice: efficient global cardiac gene transfer superior to that of AAV8.* Mol Ther, 2006. **14**(1): p. 45-53.
38. Gombash, S.E., et al., *Intravenous AAV9 efficiently transduces myenteric neurons in neonate and juvenile mice.* Front Mol Neurosci, 2014. **7**: p. 81.

39. Schuster, D.J., et al., *Biodistribution of adeno-associated virus serotype 9 (AAV9) vector after intrathecal and intravenous delivery in mouse.* Front Neuroanat, 2014. **8**: p. 42.
40. Shen, Z., et al., *Intravenous Administration of an AAV9 Vector Ubiquitously Expressing C1orf194 Gene Improved CMT-Like Neuropathy in C1orf194(-/-) Mice.* Neurotherapeutics, 2023. **20**(6): p. 1835-1846.
41. Higashi, Y., et al., *Peripheral nerve pathology in Niemann-Pick type C mouse.* Acta Neuropathol, 1995. **90**(2): p. 158-63.
42. Xie, C., et al., *AAV9-NPC1 significantly ameliorates Purkinje cell death and behavioral abnormalities in mouse NPC disease.* J Lipid Res, 2017. **58**(3): p. 512-518.
43. Hughes, M.P., et al., *AAV9 intracerebroventricular gene therapy improves lifespan, locomotor function and pathology in a mouse model of Niemann-Pick type C1 disease.* Hum Mol Genet, 2018. **27**(17): p. 3079-3098.
44. Davidson, C.D., et al., *Improved systemic AAV gene therapy with a neurotrophic capsid in Niemann-Pick disease type C1 mice.* Life Sci Alliance, 2021. **4**(10).
45. Kurokawa, Y., et al., *Gene Therapy in a Mouse Model of Niemann-Pick Disease Type C1.* Hum Gene Ther, 2021. **32**(11-12): p. 589-598.
46. Hughes, M.P., et al., *A Novel Small NPC1 Promoter Enhances AAV-Mediated Gene Therapy in Mouse Models of Niemann-Pick Type C1 Disease.* Cells, 2023. **12**(12).
47. Pentchev, P.G., et al., *A lysosomal storage disorder in mice characterized by a dual deficiency of sphingomyelinase and glucocerebrosidase.* Biochim Biophys Acta, 1980. **619**(3): p. 669-79.
48. Morris, M.D., et al., *Lysosome lipid storage disorder in NCTR-BALB/c mice. I. Description of the disease and genetics.* Am J Pathol, 1982. **108**(2): p. 140-9.
49. Shio, H., et al., *Lysosome lipid storage disorder in NCTR-BALB/c mice. II. Morphologic and cytochemical studies.* Am J Pathol, 1982. **108**(2): p. 150-9.
50. Loftus, S.K., et al., *Murine model of Niemann-Pick C disease: mutation in a cholesterol homeostasis gene.* Science, 1997. **277**(5323): p. 232-5.
51. Higashi, Y., et al., *Cerebellar degeneration in the Niemann-Pick type C mouse.* Acta Neuropathol, 1993. **85**(2): p. 175-84.
52. Wasserstein, M.P., et al., *The future of newborn screening for lysosomal disorders.* Neurosci Lett, 2021. **760**: p. 136080.
53. Patterson, M.C., et al., *Disease and patient characteristics in NP-C patients: findings from an international disease registry.* Orphanet J Rare Dis, 2013. **8**: p. 12.
54. Gaviglio, A., et al., *Infants with Congenital Diseases Identified through Newborn Screening-United States, 2018-2020.* Int J Neonatal Screen, 2023. **9**(2).
55. Administration, H.R.S. *Niemann-Pick disease*. 2024 September 2024 [cited 2025 January]; Available from: https://newbornscreening.hrsa.gov/conditions/niemann-pick-disease.
56. Surmeli-Onay, O., et al., *Prenatal-onset Niemann-Pick type C disease with nonimmune hydrops fetalis.* Pediatr Neonatol, 2013. **54**(5): p. 344-7.
57. Kelly, D.A., et al., *Niemann-Pick disease type C: diagnosis and outcome in children, with particular reference to liver disease.* J Pediatr, 1993. **123**(2): p. 242-7.
58. Kumagai, T., et al., *A case of Niemann-Pick disease type C with neonatal liver failure initially diagnosed as neonatal hemochromatosis.* Brain Dev, 2019. **41**(5): p. 460-464.

59. Shammas, H., et al., *Different Niemann-Pick C1 Genotypes Generate Protein Phenotypes that Vary in their Intracellular Processing, Trafficking and Localization.* Sci Rep, 2019. **9**(1): p. 5292.
60. Landrum, M.J., et al., *ClinVar: public archive of relationships among sequence variation and human phenotype.* Nucleic Acids Res, 2014. **42**(Database issue): p. D980-5.
61. McKay Bounford, K. and P. Gissen, *Genetic and laboratory diagnostic approach in Niemann Pick disease type C.* J Neurol, 2014. **261 Suppl 2**(Suppl 2): p. S569-75.
62. Millat, G., et al., *Niemann-Pick C1 disease: the I1061T substitution is a frequent mutant allele in patients of Western European descent and correlates with a classic juvenile phenotype.* Am J Hum Genet, 1999. **65**(5): p. 1321-9.
63. Guatibonza Moreno, P., et al., *At a glance: the largest Niemann-Pick type C1 cohort with 602 patients diagnosed over 15 years.* Eur J Hum Genet, 2023. **31**(10): p. 1108-1116.
64. Gelsthorpe, M.E., et al., *Niemann-Pick type C1 I1061T mutant encodes a functional protein that is selected for endoplasmic reticulum-associated degradation due to protein misfolding.* J Biol Chem, 2008. **283**(13): p. 8229-36.
65. Praggastis, M., et al., *A murine Niemann-Pick C1 I1061T knock-in model recapitulates the pathological features of the most prevalent human disease allele.* J Neurosci, 2015. **35**(21): p. 8091-106.
66. Yerger, J., et al., *Phenotype assessment for neurodegenerative murine models with ataxia and application to Niemann-Pick disease, type C1.* Biol Open, 2022. **11**(4).
67. Martin, K.B., et al., *Identification of Novel Pathways Associated with Patterned Cerebellar Purkinje Neuron Degeneration in Niemann-Pick Disease, Type C1.* Int J Mol Sci, 2019. **21**(1).
68. Maxfield, F.R. and D. Wustner, *Analysis of cholesterol trafficking with fluorescent probes.* Methods Cell Biol, 2012. **108**: p. 367-93.
69. Peake, K.B. and J.E. Vance, *Defective cholesterol trafficking in Niemann-Pick C-deficient cells.* FEBS Lett, 2010. **584**(13): p. 2731-9.
70. Baudry, M., et al., *Postnatal development of inflammation in a murine model of Niemann-Pick type C disease: immunohistochemical observations of microglia and astroglia.* Exp Neurol, 2003. **184**(2): p. 887-903.
71. Chiba, Y., et al., *Niemann-Pick disease type C1 predominantly involving the frontotemporal region, with cortical and brainstem Lewy bodies: an autopsy case.* Neuropathology, 2014. **34**(1): p. 49-57.
72. Cologna, S.M., et al., *Human and mouse neuroinflammation markers in Niemann-Pick disease, type C1.* J Inherit Metab Dis, 2014. **37**(1): p. 83-92.
73. Cougnoux, A., et al., *Microglia activation in Niemann-Pick disease, type C1 is amendable to therapeutic intervention.* Hum Mol Genet, 2018. **27**(12): p. 2076-2089.
74. Walker, D.G. and L.F. Lue, *Immune phenotypes of microglia in human neurodegenerative disease: challenges to detecting microglial polarization in human brains.* Alzheimers Res Ther, 2015. **7**(1): p. 56.
75. Tomita, M., et al., *Immunohistochemical phenotyping of liver macrophages in normal and diseased human liver.* Hepatology, 1994. **20**(2): p. 317-25.
76. Boenzi, S., et al., *Comprehensive-targeted lipidomic analysis in Niemann-Pick C disease.* Mol Genet Metab, 2021. **134**(4): p. 337-343.

77. Pergande, M.R., et al., *Lipidomic Analysis Reveals Altered Fatty Acid Metabolism in the Liver of the Symptomatic Niemann-Pick, Type C1 Mouse Model.* Proteomics, 2019. **19**(18): p. e1800285.
78. Elleder, M., et al., *Niemann-Pick disease type C. Study on the nature of the cerebral storage process.* Acta Neuropathol, 1985. **66**(4): p. 325-36.
79. Zervas, M., K. Dobrenis, and S.U. Walkley, *Neurons in Niemann-Pick disease type C accumulate gangliosides as well as unesterified cholesterol and undergo dendritic and axonal alterations.* J Neuropathol Exp Neurol, 2001. **60**(1): p. 49-64.
80. Tobias, F., K.C. Pathmasiri, and S.M. Cologna, *Mass spectrometry imaging reveals ganglioside and ceramide localization patterns during cerebellar degeneration in the Npc1(-/-) mouse model.* Anal Bioanal Chem, 2019. **411**(22): p. 5659-5668.
81. Maue, R.A., et al., *A novel mouse model of Niemann-Pick type C disease carrying a D1005G-Npc1 mutation comparable to commonly observed human mutations.* Hum Mol Genet, 2012. **21**(4): p. 730-50.
82. Park, W.D., et al., *Identification of 58 novel mutations in Niemann-Pick disease type C: correlation with biochemical phenotype and importance of PTC1-like domains in NPC1.* Hum Mutat, 2003. **22**(4): p. 313-25.
83. Davies, J.P. and Y.A. Ioannou, *Topological analysis of Niemann-Pick C1 protein reveals that the membrane orientation of the putative sterol-sensing domain is identical to those of 3-hydroxy-3-methylglutaryl-CoA reductase and sterol regulatory element binding protein cleavage-activating protein.* J Biol Chem, 2000. **275**(32): p. 24367-74.
84. Shieh, P.B., et al., *Safety and efficacy of gene replacement therapy for X-linked myotubular myopathy (ASPIRO): a multinational, open-label, dose-escalation trial.* Lancet Neurol, 2023. **22**(12): p. 1125-1139.
85. Ong, W.Y., et al., *Neurodegeneration in Niemann-Pick type C disease mice.* Exp Brain Res, 2001. **141**(2): p. 218-31.
86. Vance, J.E. and B. Karten, *Niemann-Pick C disease and mobilization of lysosomal cholesterol by cyclodextrin.* J Lipid Res, 2014. **55**(8): p. 1609-21.
87. Lloyd-Evans, E. and F.M. Platt, *Lipids on trial: the search for the offending metabolite in Niemann-Pick type C disease.* Traffic, 2010. **11**(4): p. 419-28.
88. Pineda, M., M. Walterfang, and M.C. Patterson, *Miglustat in Niemann-Pick disease type C patients: a review.* Orphanet J Rare Dis, 2018. **13**(1): p. 140.
89. Karten, B., et al., *Trafficking of cholesterol from cell bodies to distal axons in Niemann Pick C1-deficient neurons.* J Biol Chem, 2003. **278**(6): p. 4168-75.
90. Carcel-Trullols, J., A.D. Kovacs, and D.A. Pearce, *Cell biology of the NCL proteins: What they do and don't do.* Biochim Biophys Acta, 2015. **1852**(10 Pt B): p. 2242-55.
91. Mukherjee, A.B., et al., *Emerging new roles of the lysosome and neuronal ceroid lipofuscinoses.* Mol Neurodegener, 2019. **14**(1): p. 4.
92. Bach, G., *Mucolipidosis type IV.* Mol Genet Metab, 2001. **73**(3): p. 197-203.
93. Sangster, M.L., et al., *A blood-brain barrier-penetrant AAV gene therapy improves neurological function in symptomatic mucolipidosis IV mice.* Mol Ther Methods Clin Dev, 2024. **32**(2): p. 101269.
94. Rodriguez-Gil, J.L., et al., *Genetic background modifies phenotypic severity and longevity in a mouse model of Niemann-Pick disease type C1.* Dis Model Mech, 2020. **13**(3).

Figure 1

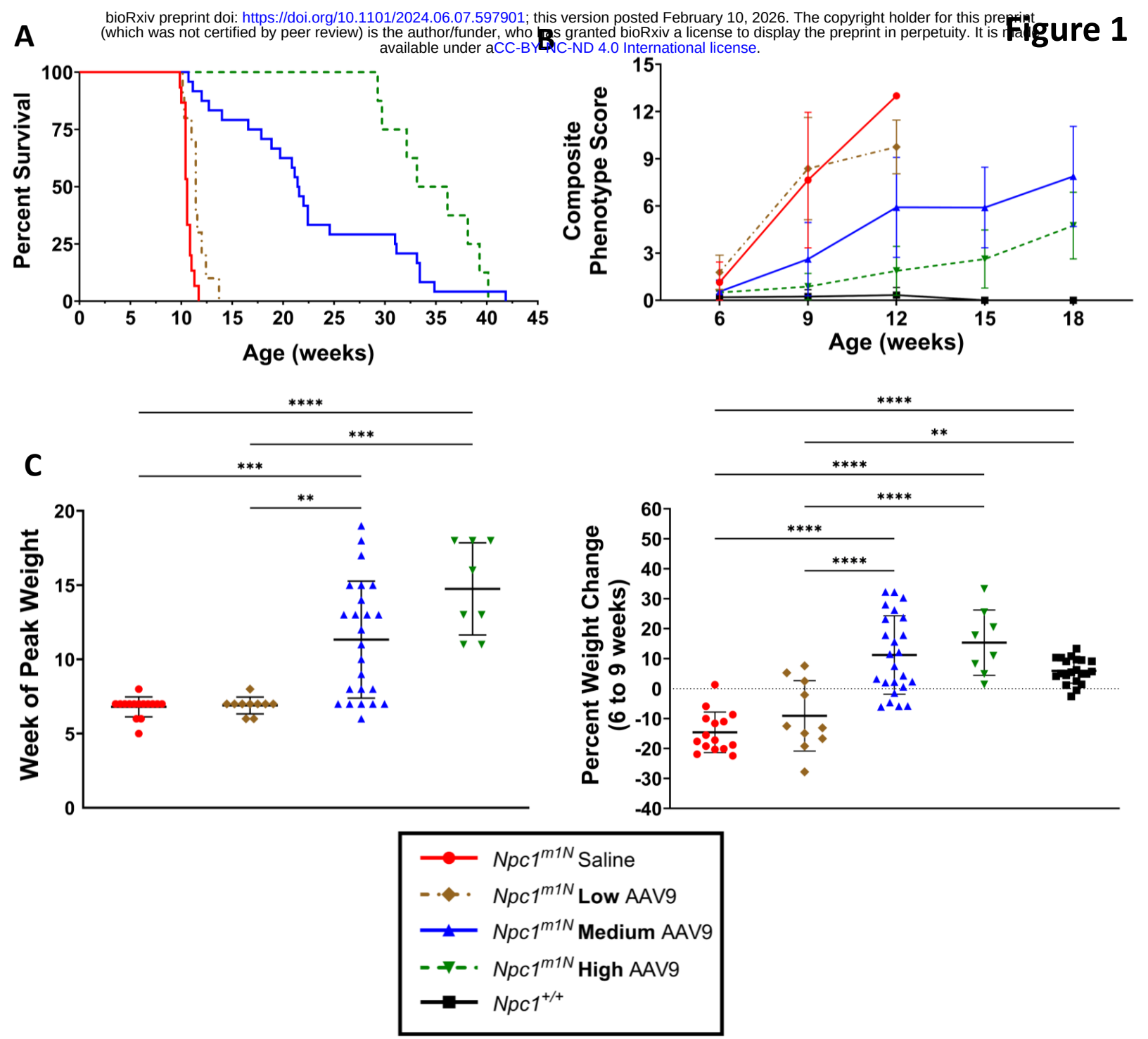

Figure 2

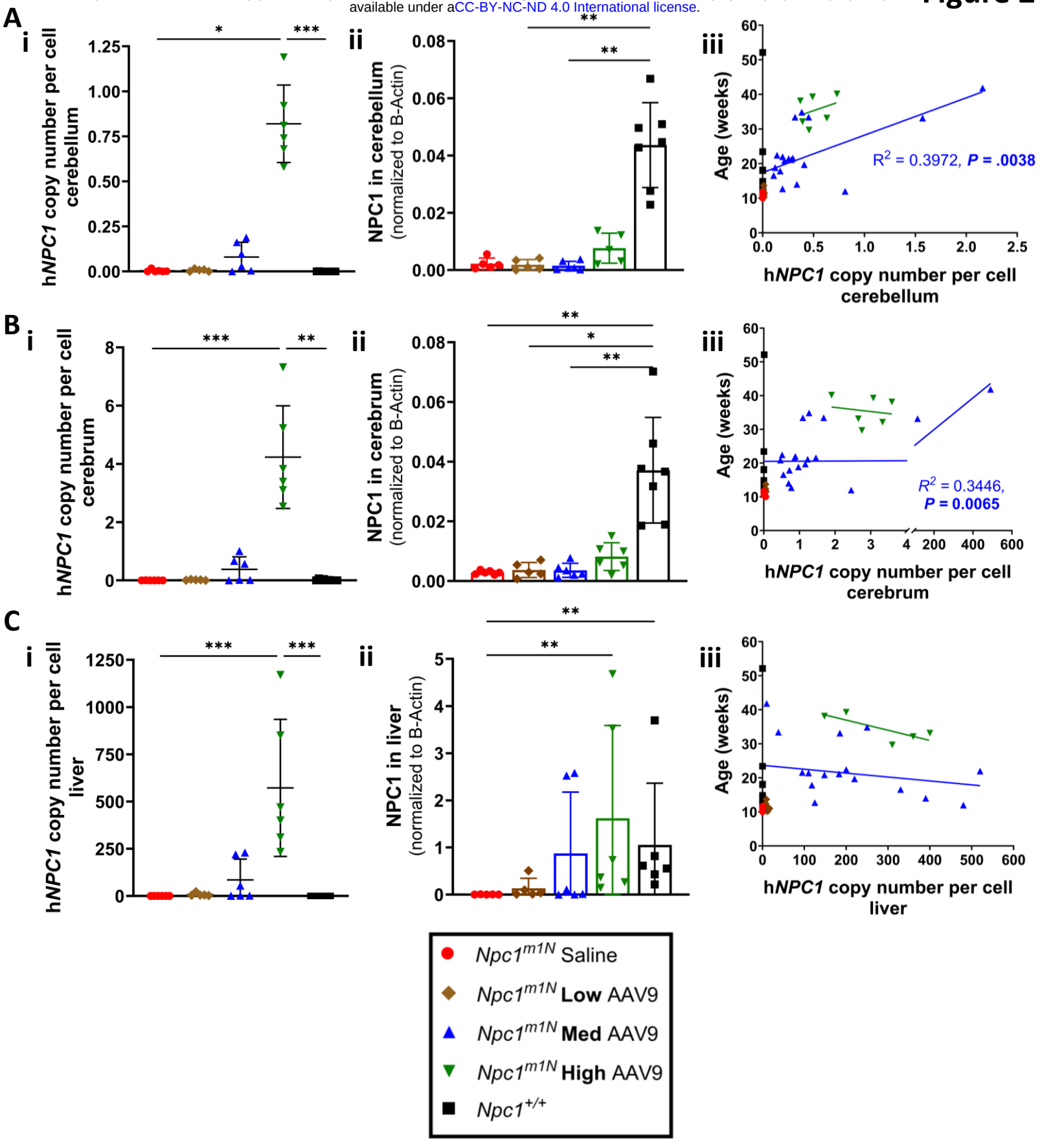

Figure 3

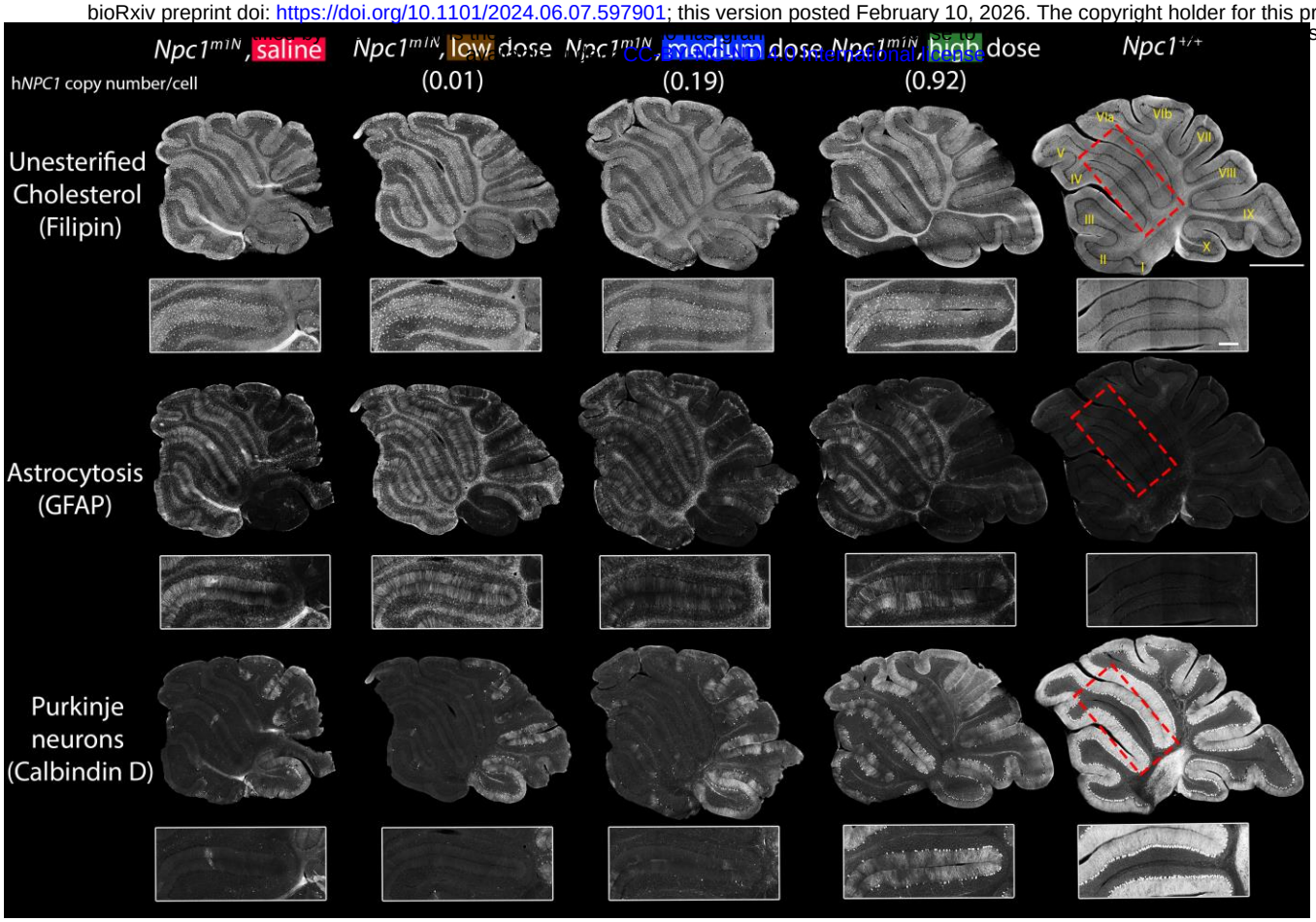

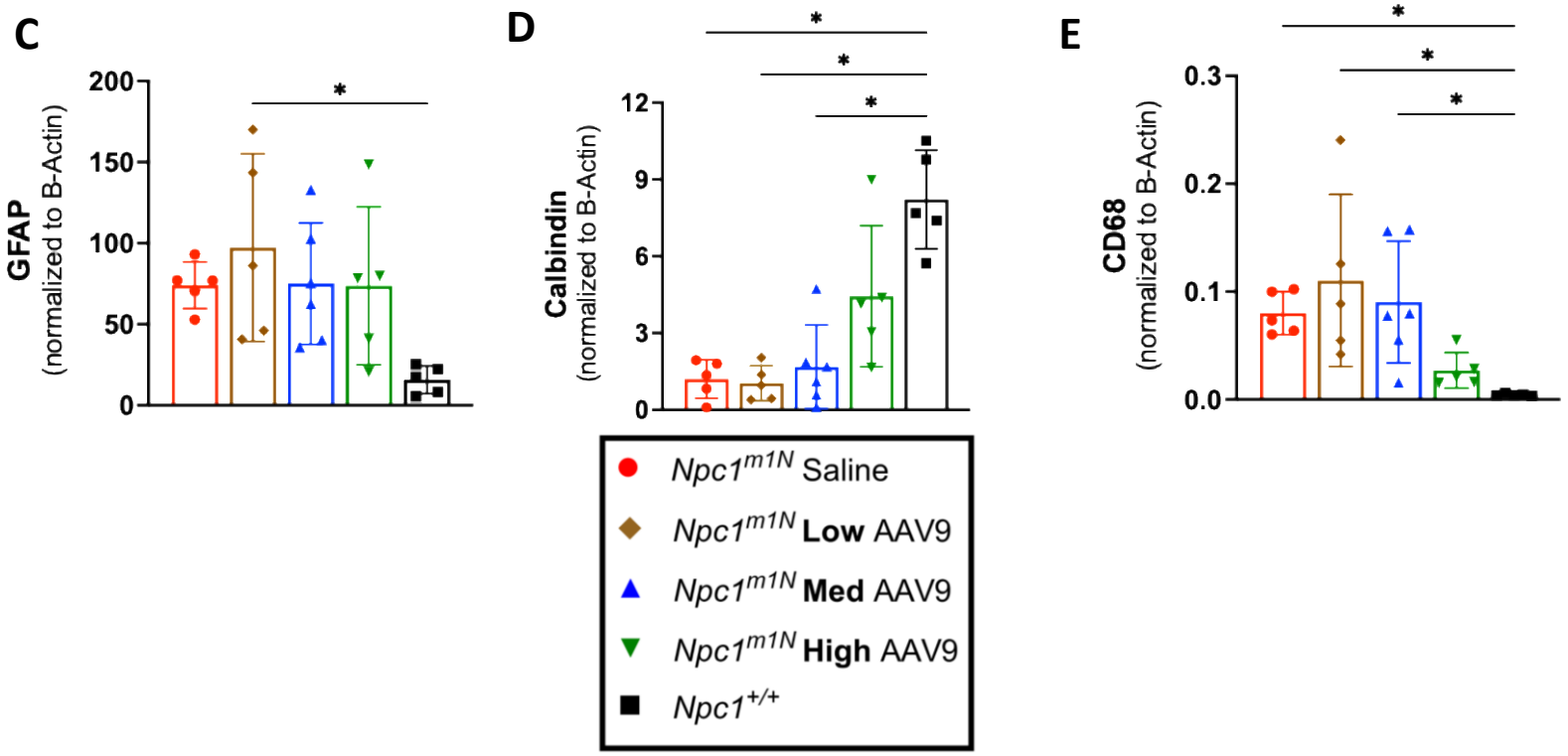

Figure 4

A

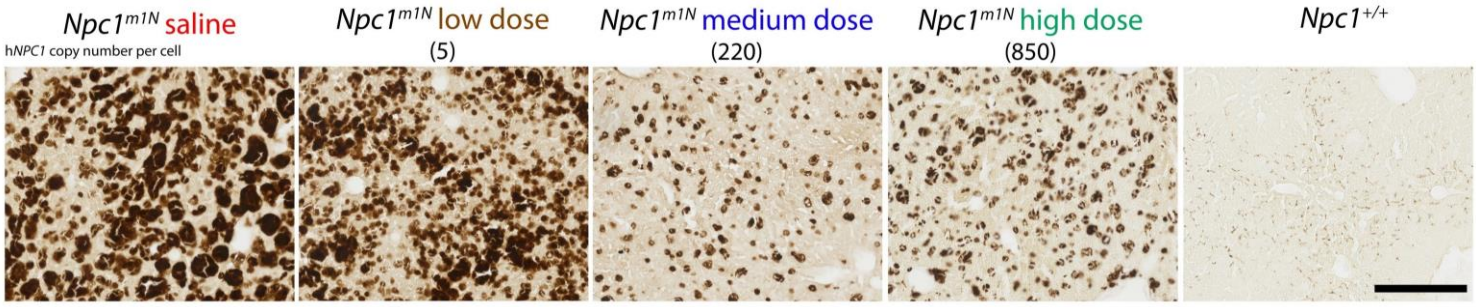

B

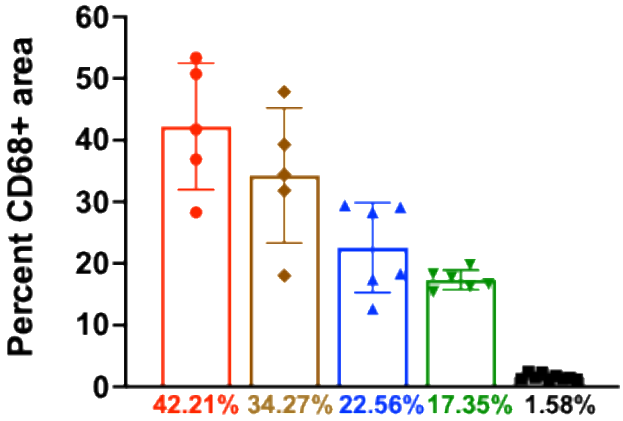

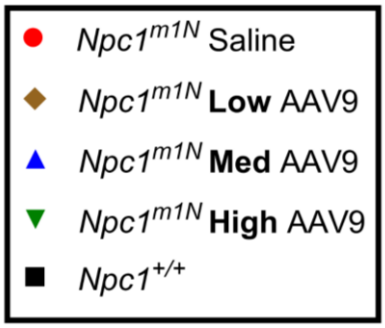

C

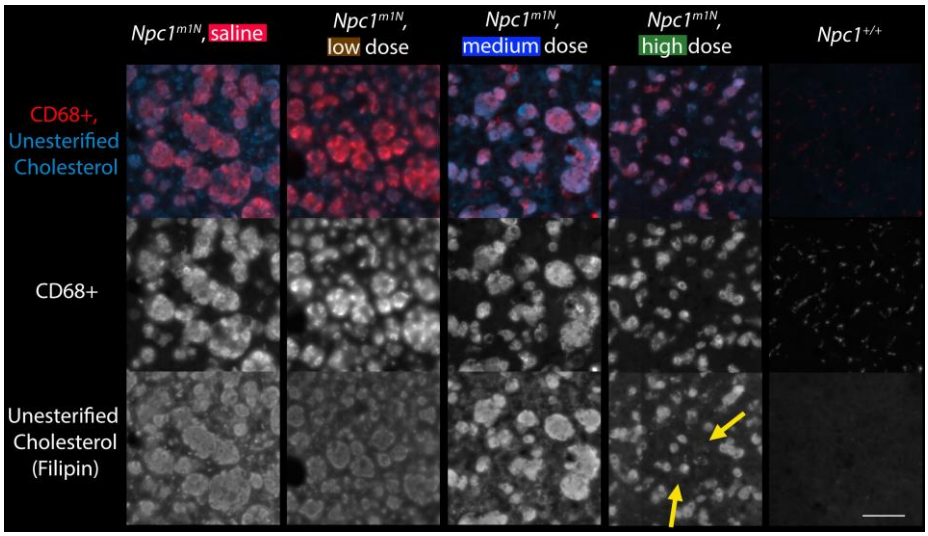

Figure 5

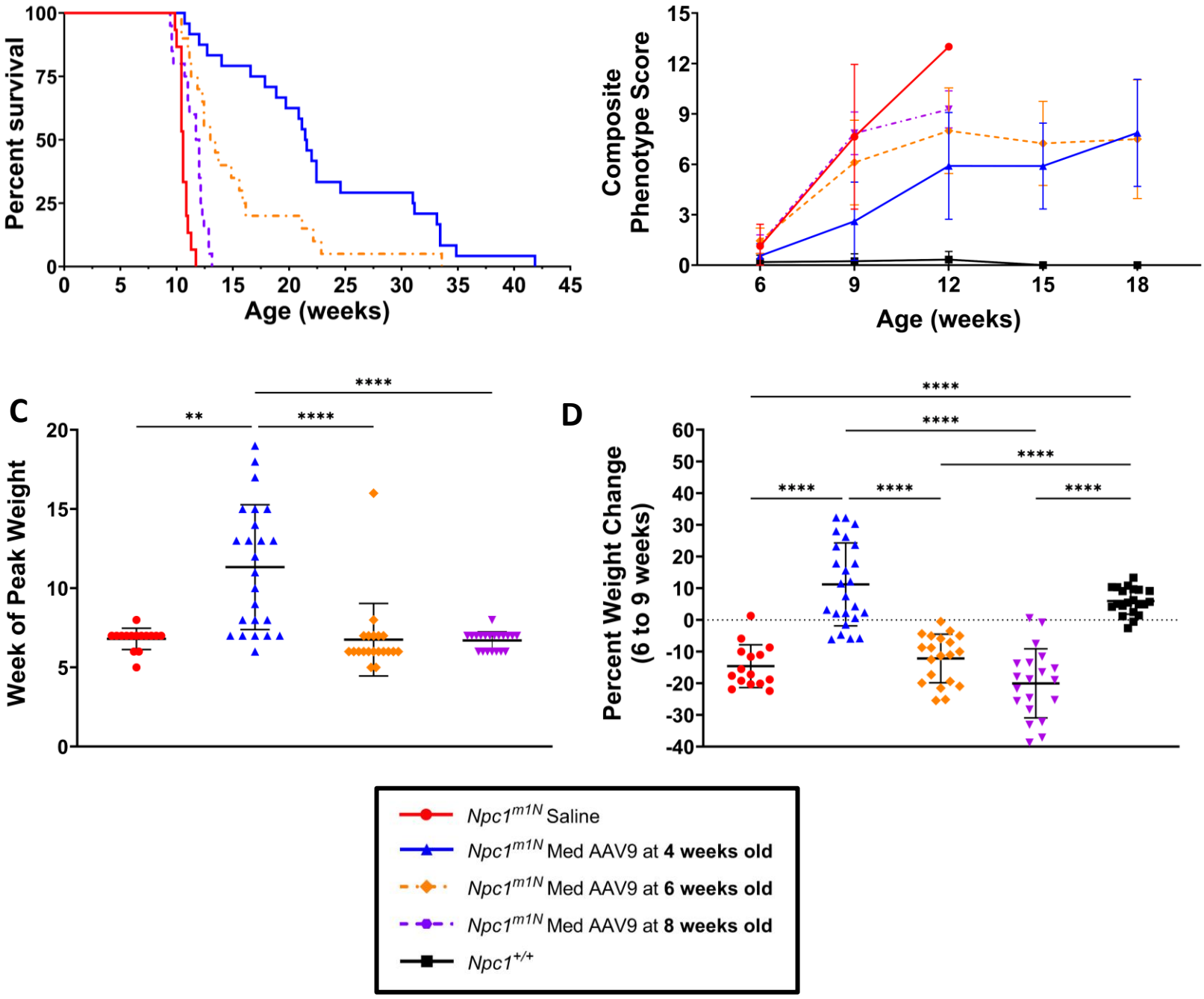

Figure 6

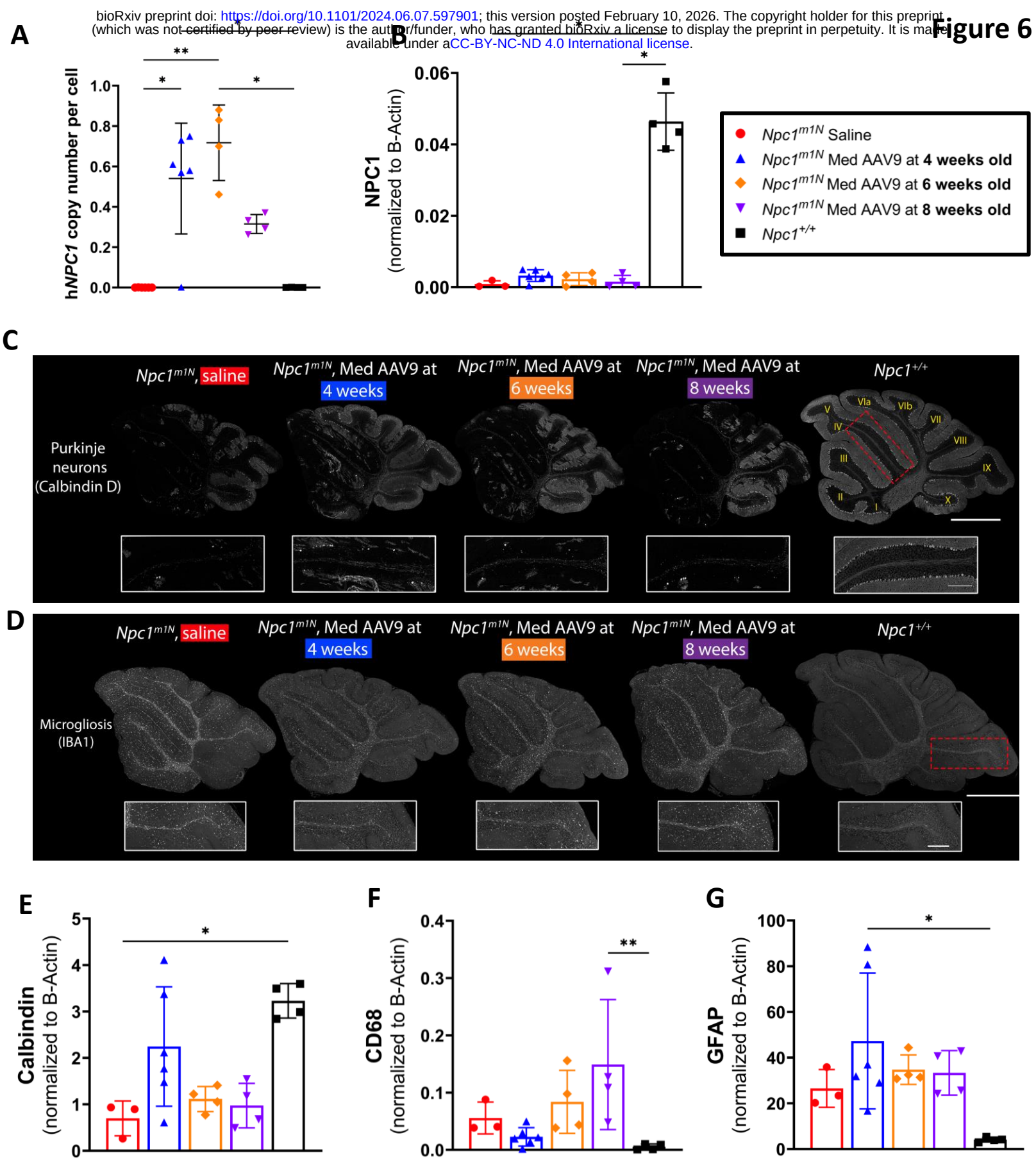

Figure 7

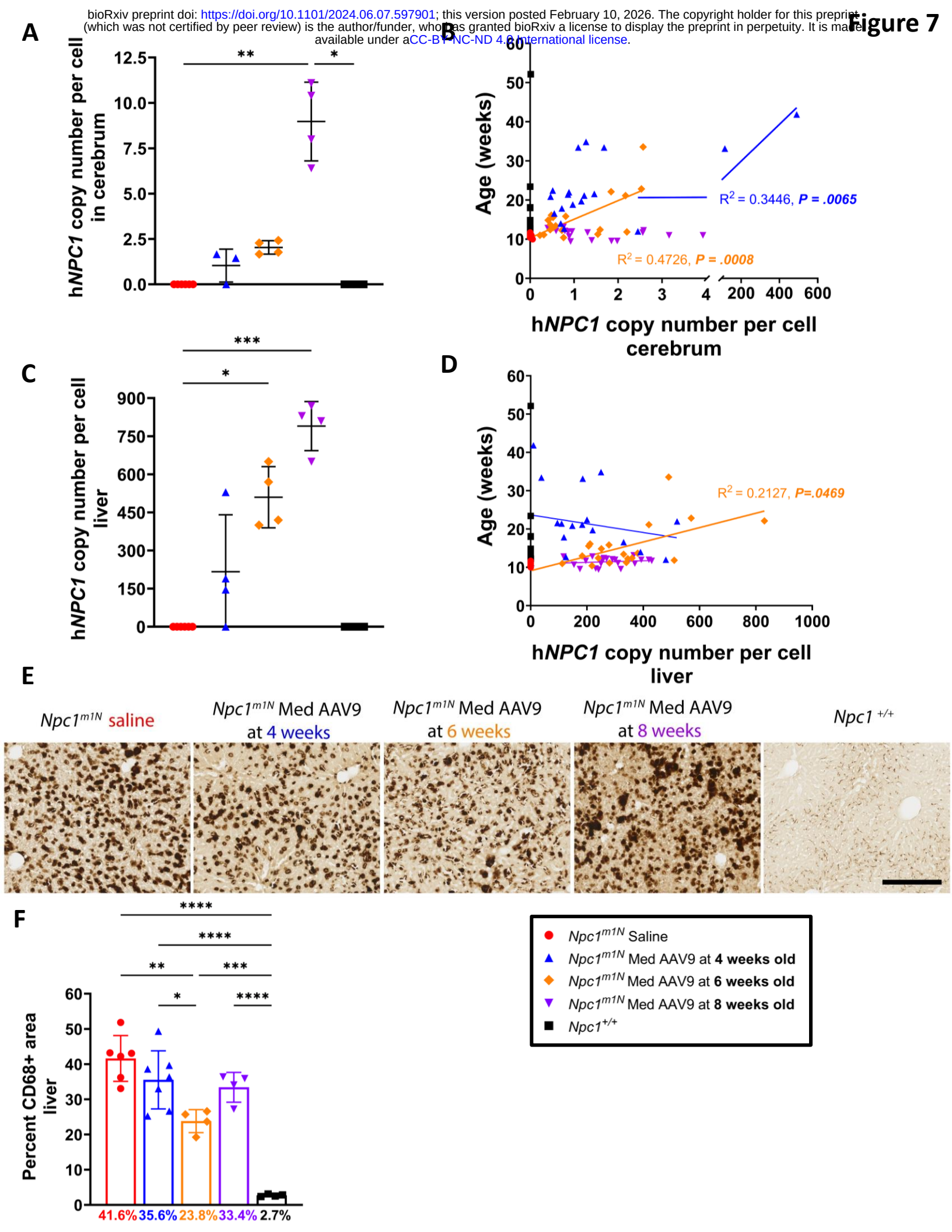

Figure 8

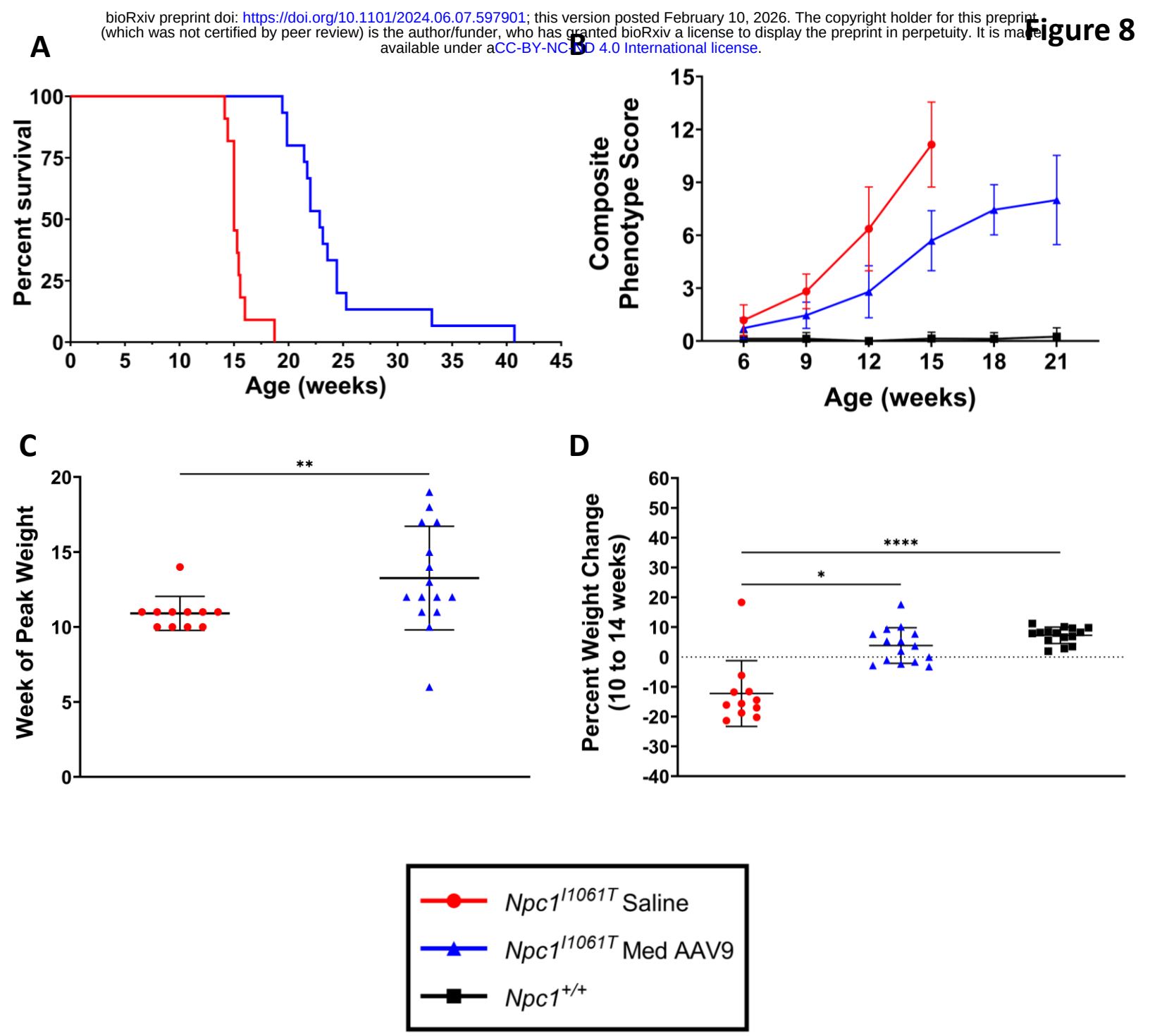

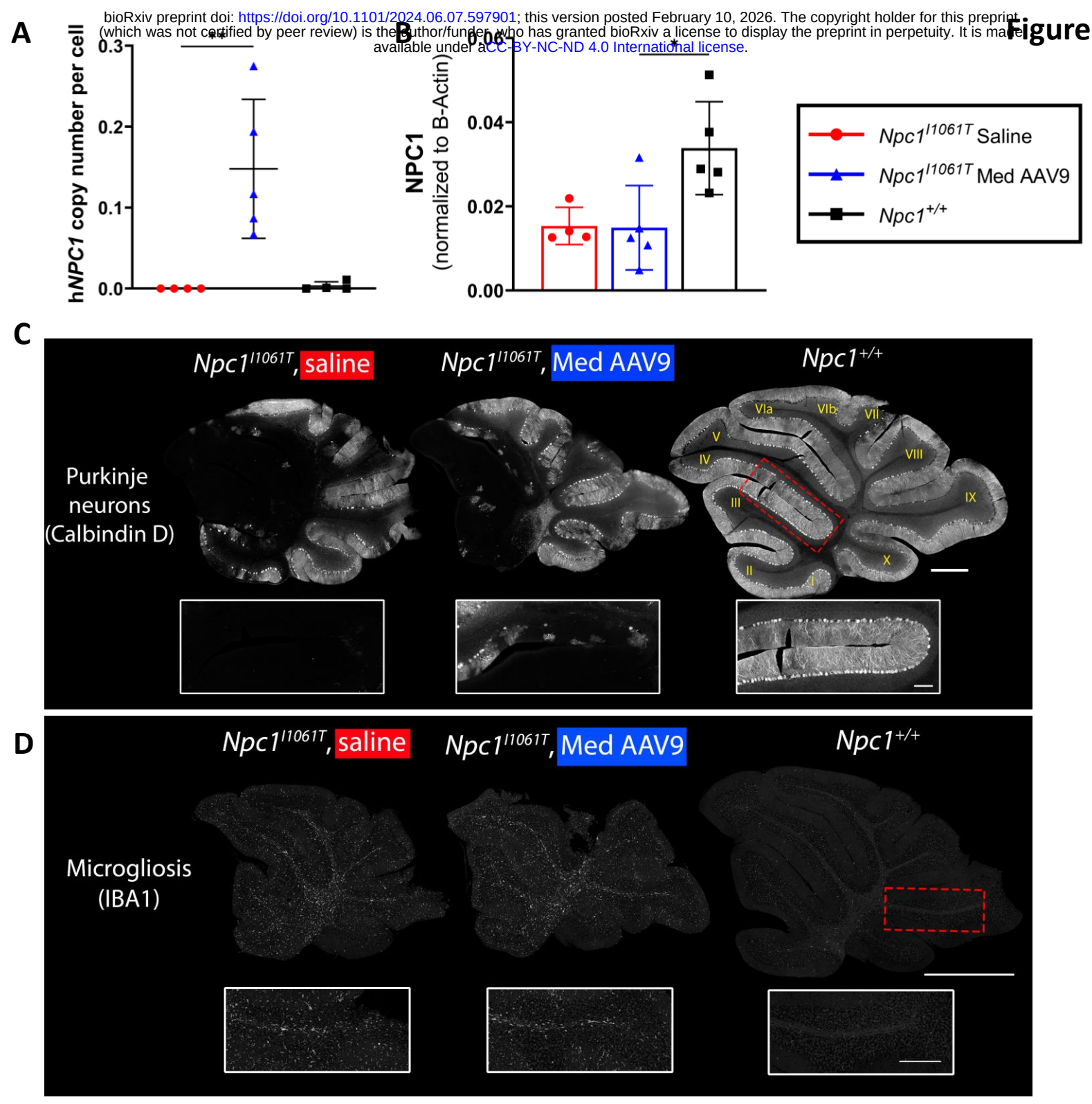

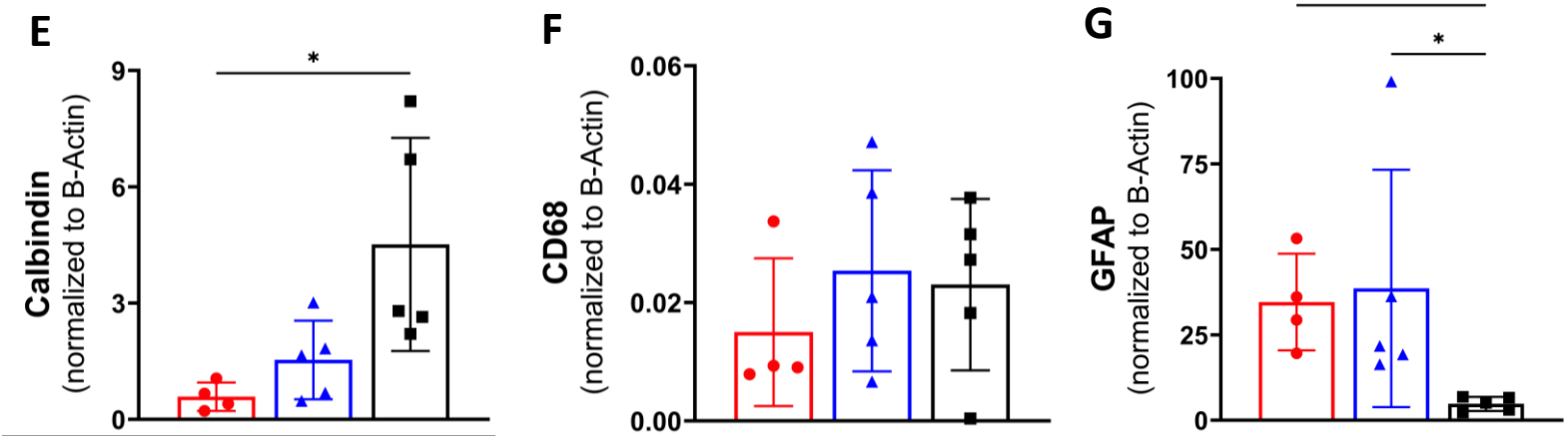

Figure 10